ADVANCED MATERIALS TECHNOLOGIES

www.advmattechnol.de

Check for updates

Silicon Photonic Platform for Passive Waveguide Devices: Materials, Fabrication, and Applications

Yikai Su, Yong Zhang, Ciyuan Qiu, Xuhan Guo, and Lu Sun*

Silicon photonics has attracted tremendous interest from academia and industry, as the fabrication of the silicon family of photonic devices is mostly compatible with the microelectronics process using complementary metal-oxide semiconductors (CMOS). Herein, three silicon-family materials are discussed: silicon, silicon nitride, and silica. In addition, hybrid integration with a 2D material, graphene, is examined. First, the material and waveguide properties are reviewed. Second, typical fabrication processes for waveguide devices are introduced. Subsequently, a variety of passive waveguide devices, operating at different physical dimensions covering wavelength, polarization, and mode, are discussed. They correspond to fixed and tunable filters, polarization beam splitters and rotators, and mode conversion and multiplexing devices. These passive waveguide devices play important roles in a wide range of applications including telecom, interconnects, computing, sensing, quantum information processing, bio-photonics, and energy.

1. Introduction

Photonic devices have found widespread applications in different fields, including information technology, physics, biology, and energy. Among the diverse materials of choice, silicon has attracted tremendous interest from academia and industry. Silicon photonics leverages the standard complementary metal-oxide semiconductor (CMOS) manufacturing process used in the microelectronics industry, thus enabling high integration density, high yield, and potentially low cost. The past two decades witnessed the rapid growth of silicon photonics research and development.[1] Design and fabrication technologies have advanced significantly, which led to foundries offering multi-project wafer (MPW) services. These international foundries include, but are not limited to, Advanced Micro Foundry (AMF) in Singapore, the Interuniversity Microelectronics Centre (IMEC) in Belgium, the American Institute of Manufacturing (AIM) photonics in the US, and the French Alternative Energies and Atomic Energy Commission (CEA)-Leti in France. Meanwhile, many fabrication labs have been built in academia with higher fabrication resolution on a smaller scale, mainly for fundamental research. While most of these labs started with silicon materials, some of them have expanded to other materials in the silicon family, such as silicon nitride (Si_3N_4). To date, silicon, Si_3N_4, and silica (SiO_2) are the three matured silicon-family materials widely employed in photonic research and development. The Si_3N_4 waveguide enables low loss and wide spectral window, suitable for resonator devices with high Q factors, for example, above $\approx 10^7$. Silica waveguides exhibit large mode sizes, compatible with those of fibers for easy coupling. Therefore, silica waveguide devices have been extensively used in conventional photonic integrated circuits (PICs).

In parallel with the boom in silicon photonics, other new opto-electronic materials have emerged. Among them, 2D materials have received considerable attention due to their nanoscale thin film properties, which do not significantly change the mode fields of silicon photonic waveguides when integrated. The 2D materials offer new possibilities to realize new functions or to improve device performance through hybrid integration with silicon photonic devices. For example, graphene is a typical 2D material that exhibits excellent performance. It was perhaps the first 2D material integrated with silicon photonics.

On the application side, a general approach to categorizing the devices is based on their operation principles in different physical dimensions. These dimensions include wavelength, polarization, and mode. Correspondingly, silicon photonic devices can be divided into filters, polarization handling devices, and mode manipulation devices.

This review paper introduces the material properties of silicon, Si_3N_4, silica, and graphene on silicon in Section 2. Section 3 discusses the optical properties of the waveguides made of these materials, covering the waveguide dimension and loss. The fabrication processes of these waveguides are illustrated in Section 4. Subsequently, Section 5 provides an overview of functional devices in different physical dimensions, including fixed and tunable filters, polarization beam splitters and rotators, mode conversion and multiplexing devices, and graphene on silicon hybrid devices. This paper limits the scope of the review to passive devices because active components need materials other than silicon, Si_3N_4, silica, and graphene. Finally, Section 6 summarizes the review. It should be noted that given the rapid technological advancements, this review may possibly omit a number of interesting developments. Overall, this paper attempts to offer a general review for researchers entering the

Prof. Y. Su, Dr. Y. Zhang, Prof. C. Qiu, Prof. X. Guo, Dr. L. Sun
State Key Laboratory of Advanced Optical Communication
Systems and Networks
Department of Electronic Engineering
Shanghai Jiao Tong University
Shanghai 200240, China
E-mail: yikaisu@sjtu.edu.cn

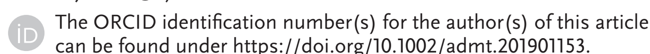
The ORCID identification number(s) for the author(s) of this article can be found under https://doi.org/10.1002/admt.201901153.

DOI: 10.1002/admt.201901153

© 2020 WILEY-VCH Verlag GmbH & Co. KGaA, Weinheim

field, and also provide abundant information and relevant references for experienced scientists and engineers to keep track of published results of their interest.

Yikai Su received his Ph.D. degree in electrical engineering from Northwestern University, Evanston, IL, USA in 2001. He worked at Crawford Hill Laboratory of Bell Laboratories and then joined the Shanghai Jiao Tong University as a full professor in 2004. His research areas cover silicon photonic devices for information transmission and switching.

Yong Zhang received his Ph.D. degree from the Huazhong University of Science and Technology, Wuhan, China. He joined Shanghai Jiao Tong University, Shanghai, China, as an assistant professor in 2015 and became an associate professor in 2019. His research areas cover silicon photonics devices, polarization, and mode devices.

Ciyuan Qiu received his B.S. and M.S. degrees from Tsinghua University, Beijing, China in 2005 and 2007, respectively, and Ph.D. degree from Rice University, Houston, Texas, in 2013. Then, he worked as a postdoc in Rice University until June 2014. Dr. Qiu joined Shanghai Jiao Tong University, Shanghai, China, in August 2014. His research interests include Silicon Photonics Devices and Circuits, Graphene Optics, and Plasmonics.

2. Materials

2.1. Silicon, Silicon Nitride, and Silica

To realize integrated passive waveguide devices with low losses, various materials based on silicon photonic platforms have been demonstrated, such as silicon, silicon nitride, and silica. The material absorption characteristics of these popular materials are shown in **Figure 1**.[2,3] The silicon material exhibits low absorption in the wavelength range of 1.1–8.5 µm, which covers the near-infrared (NIR) and mid-infrared (MIR) regions. However, silicon materials are not an option for applications in the shorter wavelength range, such as data communications at 850 nm. Silicon nitride has a wide optical bandgap that can be varied from 2.7 to 5.0 eV by changing the N/Si ratio; thus, the transparent window of silicon nitride ranges from 400 nm to the MIR range.[4] Silicon nitride is a viable solution to implement "silicon photonics" at wavelengths shorter than 1.1 µm. Silica is an attractive material for passive PICs because of its mature fabrication process, low propagation loss, and compatibility with optical (silica) fibers.[5] Silica materials exhibit low absorption in the visible range to MIR region. This study focuses on integrated passive waveguide devices in the NIR telecom band.

Table 1 lists the refractive indices, thermo-optic (TO) coefficients, and nonlinear coefficients of silicon, silicon nitride, and silica materials in the NIR range. Silicon materials exhibit the highest refractive index, leading to the highest index contrast and the most compact footprint for silicon waveguide devices. Si_3N_4 can be formed by low-pressure chemical vapor deposition (LPCVD) or plasma-enhanced chemical vapor deposition (PECVD) processes. LPCVD-based silicon nitride is close to stoichiometric Si_3N_4, and has a refractive index of approximately 2.0 in the telecom band. The optical properties of PECVD-based silicon nitride depend on the deposition conditions. A silicon-rich (higher refractive index) or nitride-rich (lower refractive index) waveguide can be achieved by changing the N/Si ratio.[4] The high TO coefficient of silicon makes silicon waveguide devices strongly sensitive to temperature variations, especially for silicon microcavity devices. On the other hand, however, due to the high TO coefficient of silicon, a silicon wavelength filter with ultra-high TO tuning efficiency and a silicon switch with ultra-low power consumption can be realized.[6,7] The TO coefficients of silicon nitride and silica are approximately one order of magnitude lower than that of silicon. The Kerr nonlinearity of silicon is large. However, it is hindered by the strong two-photon absorption (TPA) in the telecom band. Compared to silicon, silicon nitride has a negligible TPA in the NIR. Despite its lower Kerr nonlinear coefficient compared to that of silicon, silicon nitride waveguides have been used for many nonlinear applications, such as supercontinuum and frequency comb generation.[8,9] Silicon, silicon nitride, and silica materials have negligible second-order nonlinearity and Pockels effect

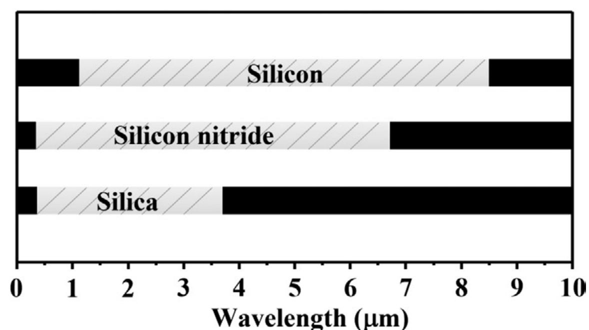

Figure 1. Material absorption characteristics of silicon, silicon nitride, and silica materials. The shaded regions represent the optical transparent window, while the black areas show the high absorption loss wavelengths.

© 2020 WILEY-VCH Verlag GmbH & Co. KGaA, Weinheim

Table 1. Optical properties of silicon, silicon nitride, and silica materials.

Material	Refractive index	TO coefficient $[K^{-1}]$	Kerr nonlinearity $[m^2 W^{-1}]$	Pockels effect
Silicon[11]	3.467	1.86×10^{-4}	4.4×10^{-18}	None
Silicon nitride[12]	≈2.0	2.45×10^{-5}	2.4×10^{-19}[13]	None
Silica[5]	1.444	0.95×10^{-5}	2.2×10^{-20}[14]	None

due to the centrosymmetric structure of the materials. Silicon-based electro-optic modulators are difficult to realize based on Pockels effect.[10]

2.2. Graphene on Silicon

Various 2D materials[15] can be seamlessly integrated with silicon waveguides without significantly affecting the mode fields. They include graphene,[16–18] black phosphorus (BP),[19–21] and tungsten disulfide (WS_2).[22–24] Among these materials, graphene, a single atom thick carbon sheet with atoms arranged in a hexagonal structure, was first studied for integrated optoelectronic devices due to its excellent optical and electrical properties.[25–29] A mono-graphene layer has a constant absorption of 2.3% over a wide wavelength range, from infrared to visible. Graphene also has a high carrier mobility (200 000 $cm^2 V^{-1} s^{-1}$ at room temperature), which is about two orders of magnitude higher than that of silicon.[16] Additionally, graphene has a high thermal conductivity (5300 W $m^{-1} K^{-1}$)[30] as well as a large Kerr coefficient ($n_2 = 10^{-12}$ $m^2 W^{-2}$).[31] The permittivity of graphene can be controlled using electrical gating.[32,33] Recently, various opto-electronic devices have been demonstrated on graphene–silicon platforms, including high-speed modulators,[16,34,35] broadband photo-detectors,[17,18,36] high-efficiency micro-heaters for tunable optical filters,[30,37] four-wave mixing processes,[31,38] and ultra-fast optical switching.[39,40]

3. Waveguide Properties

3.1. Silicon, Silicon Nitride, and Silica Waveguides

There are a variety of silicon-family optical waveguides, including nanoscale silicon wire waveguides, silicon nitride waveguides, and microscale GeO_2-doped silica waveguides. The properties of these waveguides are introduced in the following subsections.

3.1.1. Silicon Waveguides

Silicon-on-insulator (SOI) is the preferred platform for silicon waveguides in the NIR range. In the beginning, due to the limitations of the fabrication process, silicon waveguides with large cross sections were investigated to achieve low propagation losses on thick SOI wafers with thicknesses of ≈1 μm,[41] as shown in **Figure 2**a,b. Accurate phase control and low propagation loss (<0.5 dB cm^{-1}) can be easily achieved in large rib waveguides,[42] which are important for commercial applications. However, the bending radius of the rib waveguide is typically on the order of 10^2–10^3 μm,[43] resulting in large footprints and low integration density.

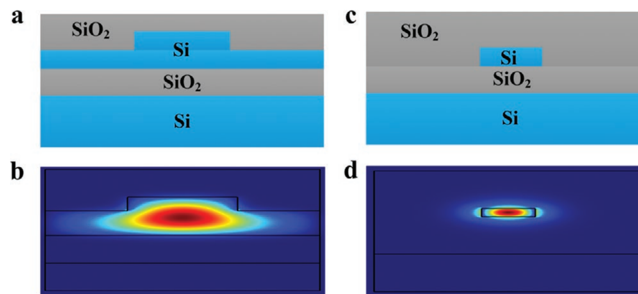

Figure 2. a) Schematic cross section and b) simulated electric field distribution of the TE_0 mode in an SOI rib waveguide. The thicknesses of the silicon guiding layer and buried oxide layer are 1.4 and 1 μm, respectively. The rib width is 1.5 μm, and the rib depth is 0.5 μm. c) Schematic cross section and d) simulated electric field (E_y) distribution of the TE_0 mode in an SOI nanowire waveguide. The thicknesses of the silicon guiding layer and the buried oxide layer are 0.22 and 2 μm, respectively. The waveguide width is 0.5 μm.

Subsequently, owing to advanced fabrication processes, nanoscale silicon wire waveguides have been demonstrated with a thickness of hundreds of nanometers, exhibiting a high index contrast of 2.47 (cladded with air) or 2 (cladded with silica) on a thin SOI wafer, as shown in Figure 2c,d. Utilizing the high index contrast, ultra-sharp waveguide bends[44] with radii <2 μm and ultra-compact silicon passive waveguide devices[45] with lengths <10 μm have been reported, enabling large-scale photonic integration. However, silicon nanowire waveguides are more sensitive to the roughness of the waveguide sidewalls or line edge roughness (LER).[46] A roughness of only a few nanometers leads to a propagation loss on the order of 1 dB cm^{-1}.[47] The propagation losses of the silicon nanowire waveguides are typically a few dB cm^{-1}, as shown in **Table 2**. Several approaches have been proposed to smoothen the waveguide sidewalls, including anisotropic wet etching,[48] optimizing the waveguide pattern,[49] and post-processing methods.[50] A waveguide propagation loss < 2 dB cm^{-1} was reported when thermal oxidation was used to smoothen the sidewalls.[51] A waveguide loss < 1 dB cm^{-1} was demonstrated when hydrogen silsesquioxane (HSQ) was used as an e-beam resist.[52] More recently, silicon nanowire waveguides were found to exhibit low propagation losses <0.40 dB cm^{-1} in the C-band, and <0.5 dB cm^{-1} at 1310 nm, when fabricated by ArF immersion lithography,[49] and hydrogen plasma and annealing,[50] respectively.

Another important issue of silicon nanowire waveguides is the sensitivity of the effective index to the waveguide width variation. A waveguide width deviation of 1 nm leads to ≈1 nm wavelength error in the transmission spectra of Mach–Zehnder interferometers (MZIs), microring resonators (MRRs), or photonic crystal (PhC) cavities.[56] The phase in the waveguide is also sensitive to the waveguide width, leading to large crosstalk in arrayed waveguide gratings (AWGs) and directional couplers (DCs). Some designs have been proposed to relax the strong dependencies on the waveguide dimension, such as

© 2020 WILEY-VCH Verlag GmbH & Co. KGaA, Weinheim

Table 2. Comparison of propagation losses for silicon nanowire waveguides.

Published year	Waveguide dimension [nm^2]	Wavelength [nm]	Loss [dB cm^{-1}]
2004[53]	445 × 220	1500	3.6
2005[54]	500 × 220	1550	2.4
2007[51]	510 × 226	1550	1.7
2008[52]	500 × 260	1520	0.92
2014[55]	500 × 220	1550	0.5
2016[49]	440 × 220	1550	0.4
2016[48]	380 × 340	1570	0.85 for TE[a)], 1.08 for TM[b)]
2018[50]	700 × 310	1310	0.37

[a)]TE: transverse electric mode; [b)]TM: transverse magnetic mode.

subwavelength grating (SWG) structures[57] and dual-core adiabatic tapers.[58]

3.1.2. Silicon Nitride Waveguides

Silicon nitride is an emerging material in the foundries and has been widely used in integrated optics. The thickness and refractive index of the silicon nitride film can be controlled by changing the deposition conditions of PECVD or LPCVD. This flexibility facilitates the combination of silicon nitride waveguide devices with silicon or other waveguide devices on a single platform to realize novel hybrid-integrated devices.

The index contrast in a silicon nitride waveguide is typically 1.0 (cladded with air) or 0.55 (cladded with silica). The propagation loss of a silicon nitride waveguide can be an order of magnitude lower than that of a silicon nanowire waveguide.[47] Several solutions have been proposed to reduce the propagation losses of silicon nitride waveguides, including annealing to remove the impurities in the silicon nitride and silica layers, smoothening the film roughness and the waveguide sidewall roughness, and properly designing the waveguide cross sections. A propagation loss of ≈0.01 dB cm^{-1} was reported in the silicon nitride waveguide at the cost of low mode confinement and large waveguide bend.[59] **Figure 3**a–c shows the simulated electric field distributions of the low-confinement, moderate-confinement, and high-confinement silicon nitride waveguides, respectively. For a low-confinement waveguide with a silicon nitride thickness of ≈100 nm, most of the optical power leaks into the cladding layer, and thus thicker layers of the buried oxide and the upper cladding are required to achieve low propagation loss. A low-confinement waveguide has been demonstrated with a propagation loss of 0.09 dB cm^{-1} at 1550 nm, enabled by the thin core layer and the 8-µm-thick buried oxide and upper cladding layers.[60] However, the bending radius of the waveguide is as large as 0.5 mm. For moderate-confinement waveguides with a silicon nitride thickness of 150–400 nm, a propagation loss of 0.30 dB cm^{-1} was reported with a reasonable curving radius of 50 µm at 1550 nm.[61] The dispersion properties can be easily controlled by adjusting the cross sections of the high-confinement waveguides with a silicon nitride layer thickness of >700 nm.[62] Thus, high-confinement silicon nitride waveguides

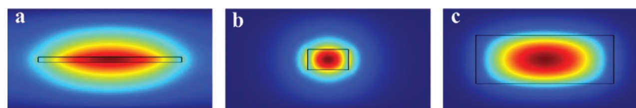

Figure 3. Simulated electric field (E_y) distributions of a) low-confinement, b) moderate-confinement, and c) high-confinement silicon nitride waveguides. The width and height of the low-confinement waveguide are 2800 and 100 nm, respectively. The width and height of the moderate confinement waveguide were 800 and 400 nm, respectively. The width and height of the high-confinement waveguide are 2700 and 950 nm, respectively. The black rectangle box represents the silicon nitride core region.

are very suitable for some linear and nonlinear optical applications, such as frequency combs and supercontinuum generation. A high-confinement waveguide has been demonstrated with a propagation loss of 0.04 dB cm^{-1} at 1550 nm.[63] **Table 3** shows the propagation losses of some reported silicon nitride waveguides, indicating that silicon nitride waveguides were successfully fabricated with low propagation losses for wavelengths ranging from 532 to 3700 nm.

3.1.3. Silica Waveguides

Silica-on-silicon optical waveguides are one of the most popular choices for PICs due to the advantages of low cost, low propagation loss, good matching to optical fibers in dimensions, and refractive index contrast.[76] Typically, with a germanium-doped silica core surrounded by silica claddings, the dimensions and materials of the silica waveguides are similar to those of the optical fibers, as shown in **Figure 4**a. To avoid high substrate leakage losses through the buried oxide layer, typical thicknesses of ≈12 µm have been used for the upper and bottom claddings.[77] The refractive-index contrast between the core and the cladding can be adjusted by changing the deposition

Table 3. Propagation losses of some silicon nitride waveguides.

Published year	Waveguide dimension [nm]	Wavelength [nm]	Bending radius [µm]	Loss [dB cm^{-1}]
2005[64]	–	1550	–	1.5
2005[65]	800 × 150	1550	500	0.11–1.45
2008[66]	2000 × 140	633	25–50	0.2
2011[60]	2800 × 100	1550	500	0.09
2013[67]	800 × 220	900	–	0.62
2013[68]	700 × 100	600	35	0.51
2013[63]	1800 × 190	1550	115	0.04
2013[69]	4000 × 2500	3700	200	2.1
2014[70]	1000 × 400	1270	–	0.32
2015[71]	2700 × 950	2600	230	0.60
2015[61]	2000 × 200	1550	50	0.3
2016[72]	1150 × 1350	1598	238	–
2017[73]	2500 × 730	1550	115	0.008 ± 0.001
2019[74]	350 × 180	532	/	1.36
2019[75]	780 × 730	1300	80	0.17

 © 2020 WILEY-VCH Verlag GmbH & Co. KGaA, Weinheim

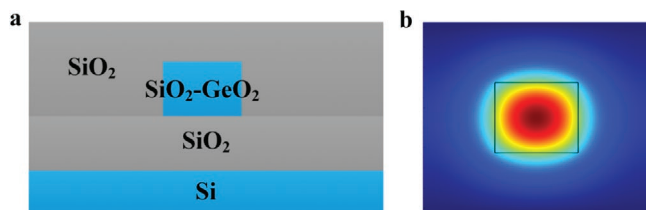

Figure 4. a) Schematic cross section and b) simulated electric field (E_y) distribution of the fundamental mode in a silica waveguide. The core size is 7 µm × 7 µm and the index contrast is 0.45%.

conditions during the fabrication process. The simulated electric field distribution is plotted in Figure 4b for a silica waveguide with a core size of 7 µm × 7 µm and an index contrast of 0.45%. The propagation loss of the silica waveguide was demonstrated to be as low as 0.017 dB cm^{-1}.[78] The fiber-chip coupling loss was lower than 0.1 dB,[5] attributed to the good mode matching between the waveguide and an optical fiber. Owing to their excellent optical performance, a large number of silica waveguide devices have been used in commercial optical equipment, such as 1 × N optical splitters[79] and AWGs.[80] The bending radius of a silica waveguide is typically tens of millimeters, leading to the large footprints of the silica waveguide devices. Therefore, it is difficult to realize large-scale PICs based on silica waveguide devices.

3.2. Graphene–Silicon Waveguides

This section focuses on the optical properties of the graphene–silicon hybrid waveguide in the telecom band. The 3D structure of the hybrid waveguide is shown in **Figure 5**a. If a graphene sheet is integrated onto a silicon waveguide with the dimensions of 500 nm × 220 nm, part of the light power (≈0.083%) is evanescently coupled to the graphene layer, as shown in Figure 5b. In this simulation, the Fermi level of graphene (E_f) was set to 0.4 eV and the permittivity was set to 2.126 + 6.038i.[81,82] If the input light wavelength is 1.55 µm (or 0.86 eV in photon energy, E_p), inter-band absorption dominates since $2E_f < E_p$ is satisfied. Thus, light in the hybrid waveguide is attenuated, and the experimental loss rate is approximately 200 dB cm^{-1}.[82] Meanwhile, through proper waveguide engineering, the loss of a hybrid waveguide can be highly dependent on the polarization state of the optical signal. Based on this principle, several polarizers based on graphene–silicon/SiO_2 hybrid waveguides have been proposed and demonstrated.[83–85]

Moreover, the aforementioned structural parameters (W, H, H_s) of the graphene–silicon hybrid waveguide should be properly designed for practical applications. Here, we consider electric-optic (EO)/TO tuning as an example to illustrate the principle, in which high efficiency as well as low loss are desired. To improve the efficiency, the light–matter interaction must be enhanced by increasing the optical power in the graphene layer. This can be achieved by reducing the width (W) and height (H) of the waveguide as well as the spacer thickness (H_s). However, if the light power in the graphene layer increases, the loss rate of the hybrid waveguide increases accordingly. Accordingly, the loss of the hybrid waveguide, expressed as loss = loss rate × L_g, also increases, which strongly affects the quality factor of a resonator based device. Thus, the modulation depth may be lowered even when the modulation efficiency is increased. Therefore, in practical applications, one needs to consider the trade-off between tuning efficiency and loss.

4. Fabrication

4.1. Silicon, Silicon Nitride, and Silica Waveguides

Over the past few years, silicon photonic platforms have become available through foundry/MPW services.[86,87] Deep ultraviolet (DUV) lithography at wavelengths of 248 nm or 193 nm has been used to define the patterns on a wafer. The lithography resolutions of the 248-nm and 193-nm DUV lights are typically 180 and 130 nm, respectively. To realize silicon devices with smaller feature sizes, several research groups have used e-beam lithography (EBL) with higher resolutions.[88] Some review papers have introduced the fabrication processes and results provided by the foundries.[89,90,91] In this paper, the authors focus on the fabrication processes using EBL.

Silicon passive waveguide devices are usually designed and fabricated on a commercial SOI wafer. The fabrication process of a typical silicon passive waveguide device is shown in **Figure 6**. For silicon chips with vertical coupling to external fibers, EBL is first used to define the grating coupler structures on the e-beam resist. Second, the patterns are transferred to the top silicon layer with an etching depth of ≈70 nm by inductively coupled plasma (ICP) dry etching. Subsequently,

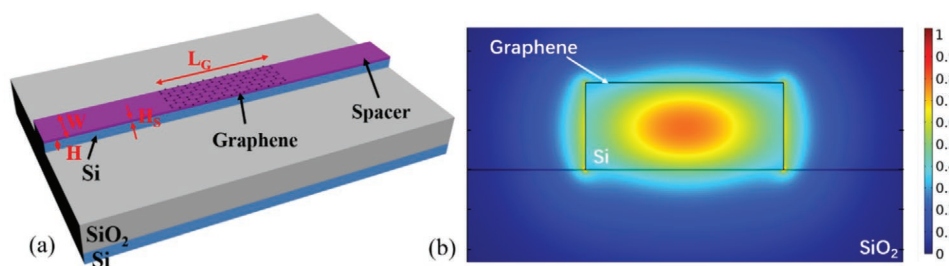

Figure 5. a) Schematic diagram of a 3D graphene–silicon integrated waveguide. W and H are the width and height of the silicon waveguide, respectively. H_s is the thickness of the spacer material between graphene and silicon. L_g is the length of the graphene material on the waveguide. b) Normalized TE mode electrical field distribution for a graphene–silicon hybrid waveguide. The dimensions of this waveguide are 500 nm × 220 nm. H_s was set to 0 nm.

© 2020 WILEY-VCH Verlag GmbH & Co. KGaA, Weinheim

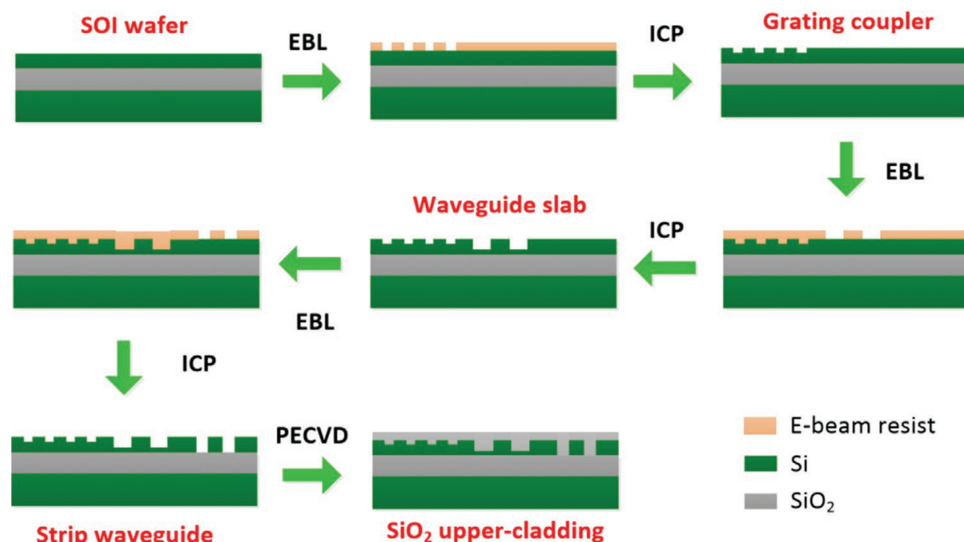

Figure 6. Schematic of the silicon device fabrication process. EBL: e-beam lithography.

the waveguide slab is defined on the silicon layer with an etching depth of ≈130 nm using EBL and ICP dry etching. The strip waveguides are then fabricated on the silicon layer with an etching depth of 220 nm. Finally, a SiO_2 layer is deposited on the wafer as the upper-cladding by PECVD.

Silicon nitride is typically deposited on a silicon substrate with a ≈3-µm-thick thermal silica layer by PECVD or by the LPCVD method to form a silicon-nitride-on-insulator wafer. For film deposition, Si–H and N–H bonds are critical issues since these bonds can act as optical absorption centers and lead to absorption losses in the NIR range. Therefore, silicon nitride films are usually grown by high temperature processes around 800 °C and then annealed at >1000 °C to break the bonds, enabling ultralow propagation loss of the silicon nitride waveguides.[65,92] The deposition process with a low temperature of <400 °C has also attracted much attention,[93] as the process provides a reasonable material quality and is compatible with CMOS back-end-of-line integration. Silicon nitride devices can be fabricated on a silicon-nitride-on-insulator wafer using EBL and ICP dry etching, which are similar to that in the silicon device fabrication process.

For silica waveguides, the SiO_2-GeO_2 core and SiO_2 cladding layers can be formed on a silicon substrate or a quartz substrate by flame hydrolysis deposition (FHD) or chemical vapor deposition (CVD) methods. After deposition, the wafers are baked in an electric furnace to approximately 1000 °C, and the glass particle layers become transparent glass layers.[5] The silica core is patterned by e-beam lithography or traditional photolithography. Subsequently, the core layer etch is implemented using a reactive ion etch (RIE) or an ICP etch. The process steps of the silica devices are also similar to that for the silicon device fabrication mentioned above.

4.2. Graphene–Silicon Waveguides

To implement graphene-integrated optoelectronic devices on a silicon platform, first, the graphene layer should be transferred onto the chip by using the wet-transfer technique, as shown in **Figure 7**. In the wet-transfer process, a polymethyl methacrylate (PMMA) layer is spin-coated on the graphene, and ferric chloride ($FeCl_3$) solution is used to etch the copper foil. The PMMA-graphene film is then moved to distilled water to rinse the etchant residue. Subsequently, the film is transferred to the substrate and the chip is dried in air overnight. Here, the PMMA can be removed by acetone and the entire chip is then covered by the graphene layer.[82] It should be noted that there are also several other schemes to etch the copper foiling, for example, by using a commercially available etchant (copper etchant Type CE-100, Transene Co.)[94] or a 0.1 M $(NH4)_2S_2O_8$.[95]

4.3. TO Tuning with Metallic Heaters

High tuning efficiency is desired for tunable silicon photonic devices.[96] Compared to electro-optic tuning, TO tuning shows the advantages of a large refractive-index tuning range and negligible optical loss.[97] Generally, TO tuning can be achieved by applying a metallic microheater on a waveguide.[98] The fabrication process of the waveguide devices with metallic heaters is shown in **Figure 8**a. After the deposition of the silica upper-cladding layer, Ti heaters and Au contact pads are fabricated on the waveguides by a lift-off process using an e-beam evaporator. A SiO_2 layer is needed between the silicon waveguide and the metallic microheater to avoid optical absorption induced by the metals. The typical tuning efficiency of this structure is ≈0.25 nm mW^{-1},[99] and is limited by the high heat capacity, which is attributed to the low thermal conductivity of SiO_2 (1.44 W m^{-1} K^{-1}).[100] Several solutions have been proposed to achieve higher tuning efficiencies, including integrating the microheater directly on the silicon slab and using suspended waveguide structures that are surrounded by air claddings.[6] The fabrication process of the suspended waveguide devices with heaters on the silicon slab is illustrated in Figure 8b. After the definition of the device patterns, Pt is sputtered on the silicon slab to form the microheaters. Au is then evaporated to define the electrical wires and contact pads using a lift-off process. Finally, the silica layer beneath

© 2020 WILEY-VCH Verlag GmbH & Co. KGaA, Weinheim

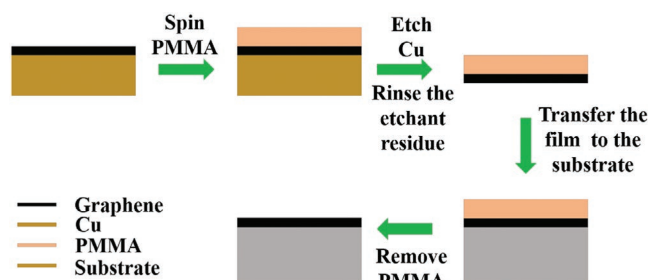

Figure 7. Graphene transfer process.

the waveguides is removed by a dilute hydrofluoric acid (HF) solution to form the freestanding structure.

4.4. TO Tuning with Graphene Heaters

The fabrication process of the graphene microheater is illustrated in **Figure 9**. Metal electrodes (i.e., Ti/Au electrodes) are deposited by EBL and the lift-off process. Then, the graphene layer is transferred onto the chip as discussed in Section 3.2. Subsequently, the graphene layer should be patterned by EBL followed by an oxygen plasma etching process to implement the micro-scale structure.[101]

5. Applications

This section reviews the typical applications of passive waveguide devices. Functional devices with different materials can be realized using the same principle; therefore, the authors use silicon as an example to illustrate the wide applications of the silicon-family passive waveguide devices. The applications of silicon photonic devices include communications, computing, quantum information processing, sensing, biology, and energy. More generally, functional devices may operate in one or more of three physical dimensions, including wavelength, polarization, and mode. Correspondingly, this section reviews three groups of passive silicon devices, that is, fixed and tunable filters, polarization beam splitters and rotators, and mode division multiplexing devices. The wavelength range of interest is the telecom band centered at 1.55 µm for silicon devices.

5.1. Fixed and Tunable Filters

5.1.1. Fixed Filters

The function of a wavelength filter is to select or block a wavelength or a set of wavelengths at the output. Silicon wavelength filters are considered one of the essential components in

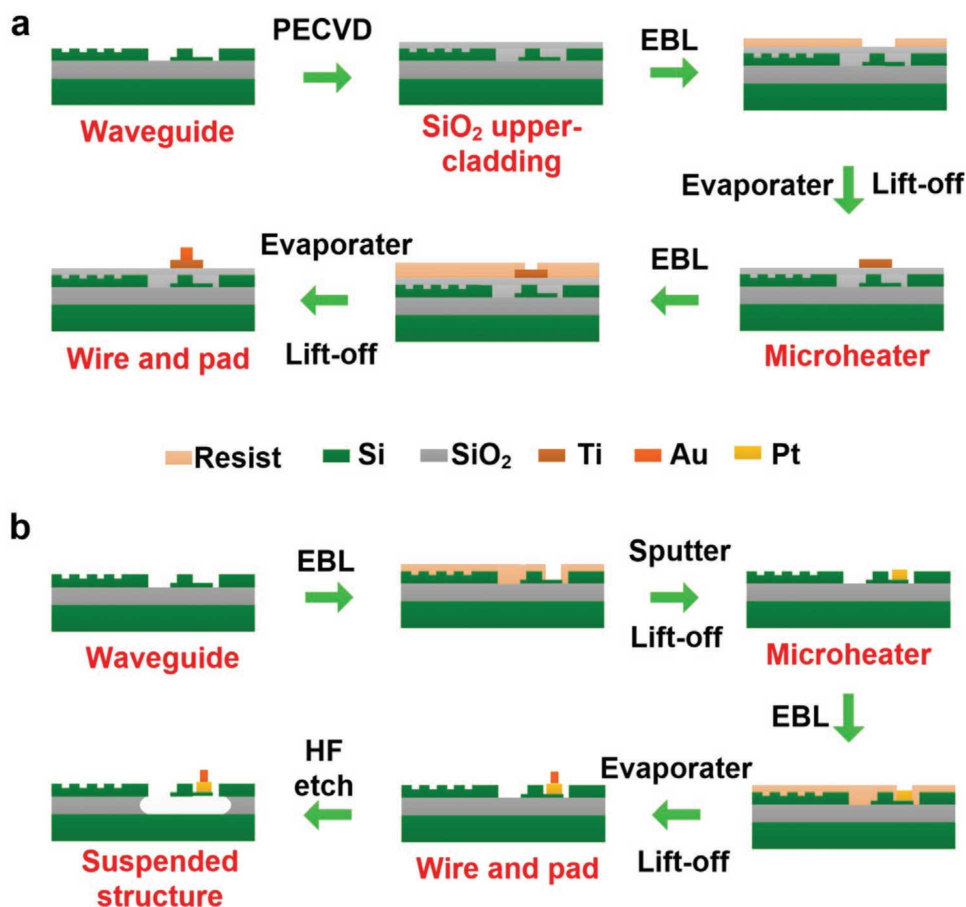

Figure 8. Fabrication processes of a) waveguide devices with metallic heaters and b) suspended waveguide devices with heaters on the silicon slab.

© 2020 WILEY-VCH Verlag GmbH & Co. KGaA, Weinheim

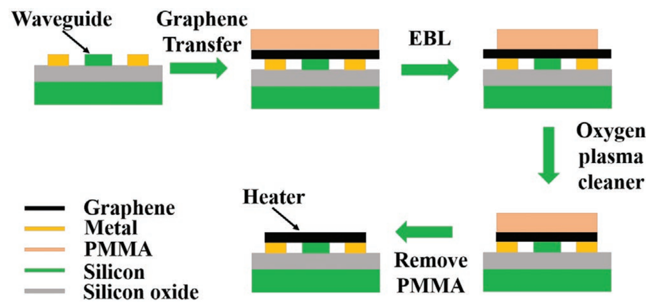

Figure 9. Graphene heater patterning process.

wavelength division multiplexing (WDM) systems. Several types of wavelength filters have been demonstrated using silicon waveguides with various basic structures including resonators, interferometers, diffraction gratings, and AWGs. Depending on the application, one can implement a wavelength filter as a single-channel drop filter or for (de)multiplexing all wavelength channels in a single operation. Drop filters based on MRR, MZI, and diffraction grating, and the (de)multiplexer based on AWG are mainly discussed herein. One main criterion of such an optical filter is the flat-top transmission band that filters/blocks the desired spectral component. The following subsection reviews some recent results on fixed and tunable filters with the four typical structures shown in **Figure 10**.

A MRR is usually composed of a waveguide ring resonator with a small ring radius, typically on the order of a few microns, coupled to input/output waveguides and add/drop waveguides (Figure 10a). This MRR filter is an infinite impulse response (IIR) filter. The filter is used as an add/drop filter, where the wavelength on resonance is extracted from other wavelength channels through the drop port. MRR-based add-drop filters are widely utilized mainly due to their compact sizes (usually 10 × 10 µm^2) and easy fabrication. However, their operation wavelength ranges are usually limited by the relatively small free spectral ranges (FSRs) (≈10 nm). Moreover, the transmission spectrum of a single MRR is expressed by the Lorentzian function with a sharp peak and a large amount of crosstalk in the rejection band. However, there are some basic structures such as series coupling, parallel coupling, and cascaded topology for the combinations of MRRs to enable synthesized and improved filter responses. A vertically triple-coupled MRR add-drop filter in a stacked configuration achieves a flat-top passband with an FSR of 25.8 nm.[102] A compact third-order coupled resonator-based filter demonstrates a large flat 3-dB bandwidth (412 GHz), an FSR of ≈18 nm and more than 18-dB out-of-band rejection at the drop port.[103] A quadruple series-coupled racetrack resonator-based filter shows a crosstalk suppression ratio of 37.2 dB, a flat-top passband with a ripple of 0.2 dB, and an FSR of 37.52 nm.[104] Another Gaussian-shaped resonance pass-band/notch filter with a bandwidth of 1–2 GHz and a high out-of-band extinction ratio (ER) of 50 dB has been demonstrated with tunable two- or five-series coupled MRRs.[105] Furthermore, a 40 cascaded MRR-based filter has been reported with a tunable and flat bandwidth range of 10–20 GHz.[106] While a complex configuration of MRRs enables a flat bandwidth for multi-channel WDM, the use of multiple MRRs requires a larger chip area, with higher consequent insertion losses (IL), and more challenges in device manufacturing.

Interferometer filters such as MZI usually make use of two DCs connected to two waveguides with different arm lengths to separate different wavelengths with constructive/destructive interference (Figure 10b), which results in a simple sinusoidal filter characteristic. This filter is a finite impulse response (FIR) filter, therefore the filtering effect comes from the interference rather than the resonance. Filters based on MZI configurations theoretically have significantly large FSRs, and can be designed to drop a single channel or multiple channels from a set of incoming channels. Several cascaded MZI adding/dropping filter configurations with flat-top transmission passbands have been proposed or demonstrated for WDM applications.[107,108] An athermal flat-topped two-stage silicon MZI filter assisted by a strip waveguide and hybrid strip-slot waveguide has been reported with a 1-dB bandwidth of 688 GHz and an FSR of

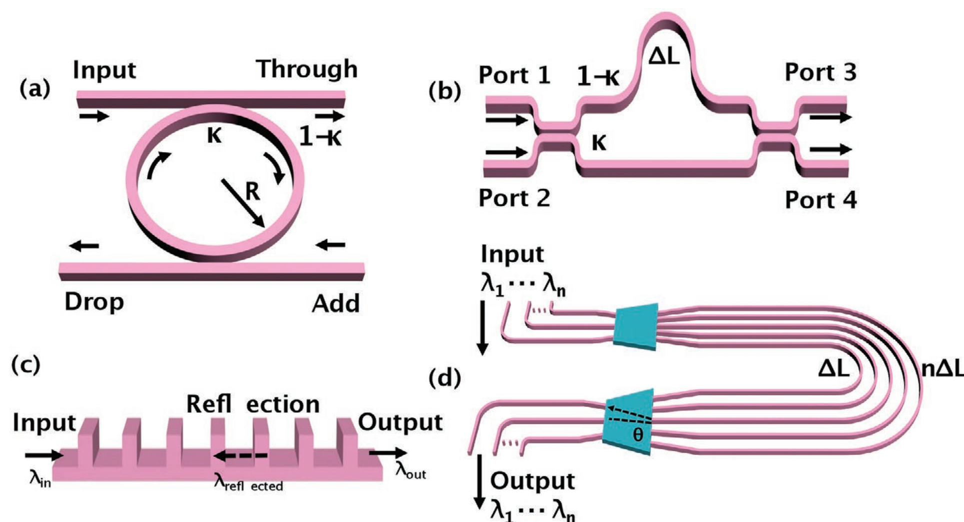

Figure 10. Wavelength filters based on a) ring resonator, b) MZI, c) diffraction grating, and d) AWG.

© 2020 WILEY-VCH Verlag GmbH & Co. KGaA, Weinheim

14.7 nm.[109] Other interesting applications of on-chip programmable pulse processors have been demonstrated by employing cascaded multimode interferometer (MMI) and MZI-MRR filter configurations for both amplitude and frequency tunings.[110–113]

Diffraction grating is based on periodic dielectric perturbations, and wavelength selectivity is achieved when the Bragg condition is met, that is, 2π phase delay between the diffraction of two adjacent grating teeth or etched grating with an effective index modulation period of $\frac{\lambda_n}{2}$ for the desired wavelength λ_n (Figure 10c). This filter is categorized as an FIR filter. However, a circulator or an isolator is usually needed in the traditional Bragg grating to prevent back Bragg reflection. Hence, various grating-assisted devices with more waveguides have been proposed to improve filter performance without the need of a circulator, including gratings, anti-symmetric gratings, and SWG-based contra-directional couplers (contra-DCs).[114–117] The contra-DCs based on periodic dielectric perturbations are analogous to waveguide Bragg gratings and have an unlimited FSR. Contra-DCs exhibit the merits of compactness, flat-top response, nearly infinite FSRs, and particularly large bandwidths (usually >10 nm). Recently, a SWG-assisted contra-DC[114] with a bandwidth of 4.07 THz has been demonstrated, but with a sidelobe suppression ratio (SLSR) of only ≈2 dB. Another improved series-cascaded apodized SWG-assisted contra-DC showed a similar large drop-port 3-dB bandwidth of 4.07 THz with much improved SLSR (>50 dB).[116] A four-channel WDM based on the asymmetric contra-DC has been demonstrated with a channel spacing of 2–3 nm and an IL of 0.23–0.58 dB.[118]

AWG is the most commonly used integrated device for multiplexing more wavelength channels. The AWG filter is also based on the interferometry mechanism and can be considered a generalization of the MZI filter to (de)multiplex a broad spectrum into multiple wavelength channels with different diffraction angle θ using a "free-space" focusing medium simultaneously (Figure 10d). The AWG wavelength filter is categorized as an FIR filter. An AWG usually has a larger footprint compared with that of an MRR when scaling in a more complex manner dictated by a combination of FSR, the number of channels, and the physical layout parameters, that is, bending radius and waveguide spacing. However, there is a trade-off between the small channel spacing and compactness with excellent performance. For silicon-based AWGs with relatively large channel spacing (e.g., Δf_{ch} = 400 GHz), excellent performances with a small footprint have been achieved.[119–121] For AWGs with smaller channel spacings (e.g., Δf_{ch} = 50, 100, 200 GHz) in dense WDM (DWDM) applications,[122–124] the device footprint increases, while the performance degrades. Recently, a compact 18-channel and 200 GHz WDM channel spacing AWG with a footprint of only 520 µm × 190 µm was realized utilizing a bidirectional AWG and MZI optical interleaver.[125]

5.1.2. Tunable Filters

Silicon benefits from a high TO coefficient of 1.86×10^{-4} K^{-1} as well as a large heat conductivity (≈149 W m^{-1} K^{-1}), and is therefore promising in realizing efficient thermally-tunable filters with high flexibility and scalability in wavelength/bandwidth/channel number to meet the more dynamic, gridless, and smart-network scenarios, such as reconfigurable optical add/drop multiplexer (ROADM). Filters with tunable bandwidths are needed in gridless ROADMs, enabling optimal spectral efficiency and optical performance monitoring.[126] Based on the previously mentioned basic wavelength filters, a variety of silicon filtering configurations with multiple basic elements have been proposed to realize wavelength and bandwidth tunability, mainly including the MRRs,[127,128] cascaded MRRs,[129–132] MZIs,[133] MZI-MRRs,[134,135] and cascaded grating structures.[136,137] However, there are always trade-offs in the performance; only a few geometries manage to achieve wide bandwidth and wavelength tunability while maintaining good off-band suppression. The following paragraphs present an overview of recent progress in tunable filters.

The MZI structures can realize wavelength tunability, but at the cost of their fixed filter shapes. A flat pass-band filter based on a cascaded MZI structure[133] has been proposed with polarization insensitivity and a wavelength tunability of 1.1 nm, a 3-dB bandwidth of 350 GHz, and an FSR of 6.09 nm. A more complex MZI structure with embedded MRRs in each branch has also been proposed to realize bandwidth tunability and wavelength tuning capability, but at the cost of limited FSR and narrow-bandwidth features. Integrated schemes based on asymmetric MZI combined with a pair of all-pass MRRs[135,138] have been demonstrated with simultaneous bandwidth and wavelength tuning. The filters offer a bandwidth tunability of 150 GHz and a full FSR wavelength-tuning range of 1.6 nm. Another bandwidth and wavelength-tunable filter scheme based on MZI with add-drop MRRs[134] exhibited an effective bandwidth tuning range of 55 GHz and a wavelength tuning range of 4 nm with an FSR of ≈8 nm. Cascaded MRR-based geometries are popular for low-loss, narrow-to-broad bandwidth tunability, and high-ER filters. Two stages of fifth-order cascaded MRRs[130] have enabled a high 100-dB passband to stop band contrast with a measured 3-dB bandwidth of 113 GHz; however, the passband is relatively lossy and the FSR is limited to 7.5 nm. Although these multi-element filters mentioned above could have good ERs, these devices exhibit relatively small tunable bandwidths (typically less than 200 GHz) and small FSRs (typically less than 10 nm), and are unable to cover the entire C-band. Recently, an ultra-high broadband tunable add-drop filter assisted by cascaded contra-DCs has been demonstrated[136] with a large bandwidth tuning range over 1 THz, a high contrast of 55 dB, and a low IL of less than 0.5 dB. Further improvements based on the loop of multimode anti-symmetric waveguide Bragg gratings[137] have enabled a wide bandwidth tunability of 1.455 THz with a flattop response and wavelength-tunable range. Some tunable optical filters with state-of-the-art tuning performances are summarized in **Table 4**.

Another important consideration is the energy efficiency of the tunable filters. The typical tuning efficiency of a silicon resonator is ≈0.25 nm mW^{-1},[139] which is related to the thermal conductivity of SiO_2 (1.44 W m^{-1} K^{-1}).[100] Various approaches have been proposed to achieve higher tuning efficiencies, including integrating the microheater directly on the nanobeam cavities or the adiabatic resonant microring[140–142] graphene microheaters on silicon PhC filters[143] and several suspended waveguide structures.[144,145] A high tuning efficiency

© 2020 WILEY-VCH Verlag GmbH & Co. KGaA, Weinheim

Table 4. Recent results of silicon-based multi-element tunable filters.

Structure and reference	Bandwidth tunability [GHz]	Wavelength tunability [nm]
MZIs[133]	–	1.1
Cascaded 2nd order MRRs[129]	225	≈3
Cascaded 5th order MRRs[130]	113	0.4
Cascaded 2nd order MRRs[131]	62.5	90
Serial MRRs[132]	94	1.7
MZI+MRRs[134]	55	4
MZI+MRRs[135]	150	1.6
Cascaded Contra-DCs[136]	1000	4
MASWBG[a)][137]	1572	13

[a)]MASWBG: multimode anti-symmetric waveguide Bragg grating.

Table 5. Recent typical energy efficient silicon tunable filters.

Structure and reference	Tuning Efficiency [nm mW^{-1}]	Tuning Range [nm]
MRR[139]	0.25	20
MRR with trenches[145]	0.9	7.75
Adiabatic resonant MRRs[141]	1.84	32.85
Suspended MRR racetrack[144]	4.8	11.5
Nanobeam[142]	0.015	6.8
Nanobeam with nanotentacles[140]	0.27	6.2
Suspended nanobeam[45]	21	43.8
PhC with Graphene microheater[143]	1.07	4

of 4.8 nm mW^{-1} was achieved in a silicon racetrack MRR with air trenches, but at the cost of a slower tuning speed of 170 µs.[144] Most power-efficient devices show multiple resonances in an operation band. High tuning efficiency with a single resonance over a wide range is highly desirable for silicon tunable filters. A high tuning efficiency of 21 nm mW^{-1} has been demonstrated[45] with a single-resonance continuous tuning range of ≈43.9 nm using a suspended silicon PhC nanobeam filter. Properties of typical energy-efficient silicon tunable filters are summarized in **Table 5**.

5.2. Polarization Handling Devices

Polarization handling devices can solve the issue of high birefringence in silicon-based waveguides.[146] They include polarization beam splitters (PBSs), polarization rotators (PRs), and polarization splitter-rotators (PSRs) as key components in polarization diverse photonic circuits. In the following subsection, some results on the PBSs based on silicon photonic platforms are presented, following which the PSRs. which combine the functions of PBSs and PRs, are reviewed.

5.2.1. PBSs

PBS is a basic element for a variety of applications, and is used to split the two orthogonal polarizations of TE and TM in silicon-based waveguides.[147,148] Several types of PBSs have been demonstrated in silicon waveguides and silicon nitride waveguides using various structures, such as DCs,[149,150] gratings,[151,152] sub-wavelength structures,[153] MMIs,[154,155] and PhC.[156] Some of the relevant works are summarized in this subsection.

The DC is a popular structure for PBSs due to its simple design. The coupling length for TM polarization is much shorter than that for TE polarization. Thus, the TM polarization is coupled to the neighboring waveguide, while the TE light still propagates along the input waveguide. A PBS with a footprint of 7 µm × 16 µm was demonstrated using a symmetrical DC with two identical silicon nanowire waveguides.[157] The polarization ER is approximately 15 dB. For a symmetrical DC, coupling of the TE-polarized light occurs, leading to low polarization ER. A higher ER can be realized by cascading the DC structure at the cost of a large footprint and a narrow bandwidth. Using an asymmetrical DC (ADC) is a good option to achieving a higher ER.[158] In the ADC structure, the phase-matching condition can be satisfied for only one polarization, while there is negligible coupling for the other polarization due to the strong birefringence. PBSs have been theoretically proposed using an ADC with silicon strip waveguides and a nanoslot waveguide.[159,160] A PBS based on an ADC having a 70-nm taper-etched waveguide and a slot waveguide has been experimentally demonstrated with an ER of >25 dB from 1462 to 1582 nm.[161] A bent DC is another type of ADC.[162,163] Several PBSs based on bent DCs have been reported with good results.[164–166] A high-performance PBS is demonstrated with an ER > 35 dB based on cascaded bent DCs.[167] The fabrication tolerance of the core-width variation is as large as ± 40 nm. A genetic algorithm has been used to optimize the PBS with an ADC structure for ultra-broadband operation.[168]

Grating-assisted contra-DC is another good choice to realize PBSs. A compact PBS based on GACCs was proposed theoretically.[169] Such a PBS is advantageous in that it does not require stringent phase matching and coupling length conditions.[170] A detailed study of the PBS was performed in terms of design, fabrication, and tolerance to width and coupling length variations.[152] However, its working bandwidth is limited (≈20 nm). Recently, a PBS was demonstrated using an anti-symmetric sidewall Bragg grating in a multimode silicon strip waveguide, showing a wide bandwidth of 64 nm.[171]

Subwavelength structures or metasurfaces enable 2D artificial materials with subwavelength feature sizes, allowing complete control of the phase, amplitude, and polarization of light beams.[172] Several PBSs have been realized based on SWGs,[173–175] inverse design method,[176] and anisotropy-engineered metamaterials.[177,178] The working bandwidth is limited for ADC-based PBSs, as the wavelength shift leads to variations in both the effective index and the coupling strength. A PBS was proposed and demonstrated through "effective

© 2020 WILEY-VCH Verlag GmbH & Co. KGaA, Weinheim

Table 6. Results of various PBSs.

Structure and reference	Loss [dB]	ER [dB]	Footprint [μm^2]	Schematic illustration
Symmetrical DC[157]	0.5	15	7 × 16	
ADC[159]	–	>10	1.5 × 6.9	
Asymmetrical partially-etched DC[161]	0.22	30	1.5 × 11	
Bent DC[167]	0.35	35	6.9 × 20	
Contra-DC[152]	<1	30	1.2 × 27.5	
Multimode Bragg gratings[171]	2	34	1.5 × 20.35	
Hetero-anisotropic metamaterials[177]	<1	>20	1.9 × 12.25	

medium anisotropy" to break the bandwidth bottleneck, instead of using "configuration asymmetry."[177] The PBS exhibits a high ER of >20 dB and a large bandwidth of >200 nm. **Table 6** shows the results of some reported silicon PBSs.

5.2.2. PSRs

PSRs combine polarization splitting and rotation simultaneously to realize ultra-compact polarization diversity circuits. For a waveguide-type PSR, an asymmetrical cross shape is required to break the waveguide symmetry. Several types of silicon-based PSRs have been reported based on various structures, such as DCs,[179,180] MMI,[181] Y-junction,[182] sub-wavelength structures,[183,184] and slot waveguides.[185]

Generally, there are two types of PSRs: mode coupling- and mode evolution-based PSRs.[186] Some of the relevant works are summarized in this subsection. For mode-evolution-based PSRs, one method is to convert the TM_0 mode into the TE_1 mode in a mode-evolution waveguide; subsequently, a mode converter is used to convert the TE_1 mode to the TE_0 mode. The conversion between the TM_0 mode and the TE_1 mode requires a mode hybridization region in a high index-contrast optical waveguide with an asymmetrical cross section, such as a T-shaped cross-section waveguide,[187] an adiabatic taper waveguide with air cladding,[188] or a rib waveguide with SiO_2 cladding.[182,189] The mode converters used in the PSRs can be realized by many structures, including ADC,[179] asymmetrical Y-junction,[182] and S-bend waveguide.[187] A silicon PSR was demonstrated with a TM_0-TE_1 polarization rotation and a TE_1-TE_0 mode converter,[188] and the remaining TM_0 mode was filtered by a bent DC. The ER was >30 dB and the IL was <1 dB for the device.

For a mode-coupling-based PSR, cross-polarization coupling can occur if two orthogonal modes have equal effective refractive indices and optical paths, and the device structure breaks the vertical and horizontal symmetries. Thus, one polarization can be converted to the other one. Efficient PSRs based on the cross-polarization coupling effect are realized by breaking the vertical symmetry with air as the top-cladding material. IL < 0.6 dB and a crosstalk value of −12 dB were achieved with an ADC with a coupling length of 36.8 μm.[190] In order to realize a fabrication-error-tolerant PSR, a tapered DC can be applied to achieve similar high polarization conversion efficiencies with a coupling length of 140 μm.[191] A bent DC was used to realize an ultra-compact silicon PSR with a coupling length of 8.77 μm.[45] To integrate with active silicon devices, SiO_2 is required as the top cladding. A highly efficient silicon PSR was reported based on a double-etched DC with SiO_2 upper-cladding.[192] However, the PSR is sensitive to fabrication variation, and the bandwidth is limited. A linearly tapered DC can be used to realize a PSR with high fabrication tolerance and large bandwidth.[193] The coupling length is ≈700 μm to achieve adiabatic coupling. Recently, a silicon PSR with a short coupling

© 2020 WILEY-VCH Verlag GmbH & Co. KGaA, Weinheim

Table 7. Results of various PSRs.

Structure and reference	Loss [dB]	ER [dB]	Footprint [μm^2]	Schematic illustration
Adiabatic tapered waveguide[179]	–	10	≈5 × 71	
Adiabatic tapered waveguide and bent DC[188]	0.57	30	≈5 × 47.5	
ADC[190]	0.6	12	≈2 × 36.5	
Asymmetrical tapered DC[191]	≈1	–	≈2 × 140	
Bent DC[45]	1	18	≈6 × 8.77	
Partially etched DC[192]	0.5	20	≈2 × 27	
Linearly tapered and Partially etched DC[193]	0.33	19	≈2 × 700	
Nonlinearly tapered and Partially etched DC[194]	1.4	18	≈2 × 129	
SWG DC[196]	1.5	13	≈2 × 55	

length of 129 μm and high fabrication tolerance has been demonstrated using a nonlinearly tapered partially-etched DC.[194] In addition, sub-wavelength grating waveguides can be employed to realize fabrication-tolerant PSRs.[195,196] The devices achieved a remarkable tolerance to fabrication deviation of up to ±40 nm, while the tolerance of several conventional devices was on the order of ±10 nm. **Table 7** shows the results of some reported silicon PSRs.

5.3. Mode Conversion Devices

Mode conversion devices are key components in on-chip mode division multiplexing systems. An ideal mode converter is supposed to convert a given spatial mode to any other desired mode with low IL, low crosstalk, broad bandwidth, short length, and large fabrication tolerance. Significant efforts have been devoted to realizing such mode converters in the past years. The working principles of the mode conversion devices can be divided into the following categories:

a) Phase matching technique: The mode in a narrower waveguide has the same effective refractive index as that in a wider waveguide. Phase matching is achieved between the two modes propagating in the waveguides, resulting in high-efficiency conversion between these two modes (**Figure 11**a).
b) Beam shaping technique: The input beam is split into two beams in the upper and lower branches. The beam in the upper branch has an excess phase compared to that in the lower branch owing to the optical path difference. The desired mode profile is formed at the joint of the two branches where the two beams in the separate branches are combined. (Figure 11b).
c) Constructive interference of coherent scattering: The input mode evolves into multiple high-order modes that interfere

© 2020 WILEY-VCH Verlag GmbH & Co. KGaA, Weinheim

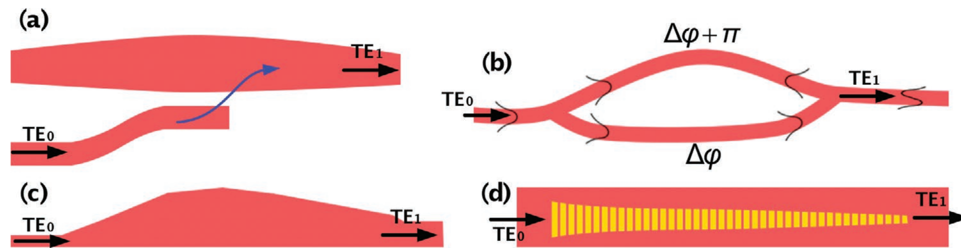

Figure 11. Mode conversions based on a) phase matching in ADC, b) beam shaping in multiple branching waveguides, c) constructive interference of coherent scattering in the exotic taper structure, and d) phase gradient induced by the optical antennas on top of the dielectric waveguide.

with each other in the conversion region. As a result, a specific mode profile can be obtained at the output end of the interference area (Figure 11c).

d) Metasurface-induced gradient phase: By imposing refractive-index perturbation on a dielectric waveguide, an excess phase gradient can be introduced along the direction of propagation, which assists the conversion between two specific modes in the waveguide (Figure 11d).

The conversion between two modes can be described by the following mode-coupling equations:

$$-\frac{\partial A}{\partial z} = i\kappa_{ab} B e^{i(\beta a - \beta b)z}$$
$$-\frac{\partial B}{\partial z} = i\kappa_{ba} A e^{i(\beta b - \beta a)z} \quad (1)$$

where A and B are the amplitudes of waveguide modes a and b, respectively; β_a and β_b are the propagation constants of the two modes; and κ_{ab} and κ_{ba} represent the exchange coupling coefficients between modes a and b, respectively. According to these equations, high-efficiency mode conversion occurs between modes a and b when the difference of the propagation constants $\beta_a - \beta_b$ is nullified, that is, phase matching is achieved for the target modes in the waveguide. There are many approaches to fulfilling the phase-matching condition in practice. Mode conversion was proposed in an adiabatic taper based on the phase-matching technique.[197] The device has a large fabrication tolerance and broad bandwidth owing to adiabaticity. However, a long interaction distance is required to satisfy the adiabaticity criterion. The length of the adiabatic taper can be shortened by applying an approach called "shortcuts to adiabaticity."[198,199] Another phase-matching technique based on ADCs has been used to realize a four-channel mode (de)multiplexer.[200] ADCs have also been used to build an on-chip WDM-polarization division multiplexing (PDM)-mode division multiplexing (MDM) optical switch.[201] A MDM and WDM circuit was implemented on a Si_3N_4-on-silica platform, where 30-Gb/s transmissions for the three modes were demonstrated.[202] ADCs were also employed to build a WDM-compatible multimode switch that routed four data channels with crosstalk < −16.8 dB.[203] The bit error rates were below 10^{-9} while routing 10-Gb s^{-1} data. To improve the fabrication tolerance, and thus, scale the mode channel number, SWGs were used to construct an 11-mode (de)multiplexing (TE_0-TE_{10}) device.[204] Low crosstalk values (−15.4 to −26.4 dB) and IL (0.1–2.6 dB) were measured for all 11 channels at 1545 nm. An adiabatic DC based on the SWG was also presented to realize a TE_0-to-TE_{12} mode converter with a conversion efficiency better than −1.5 dB over a 75-nm bandwidth.[205] Mode conversion devices based on ADCs possess the advantage of high performance and scalability of the number of channels, at the cost of the precise requirement of the coupling length and coupling strength as well as the relatively long conversion length. Other mode conversion devices based on phase matching include directional grating couplers and contra-dir÷onal grating assisted couplers.[206–208] Since they are resonant coupling devices with relatively low coupling coefficients, the mode converters are usually tens of microns in length with the bandwidths limited to several nanometers.

The beam shaping technique is a straightforward method for mode conversion. Waveguide modes in separate branches with the same or different phases can be combined to form the desired mode in the bus waveguide. Mode-order conversion between the four modes has been demonstrated by controlling the mode evolution in the multimode branching waveguides.[209] The length of the device reached several millimeters. By introducing the MZI structure, a similar mode-order converter was constructed to realize the zeroth-order to first-order mode conversion in a length of ≈20 µm.[210] A large bandwidth can be obtained using differential waveguides in the MZI.[211] The same strategy can be applied in the asymmetric graded-index PhCs, where beams following different ray trajectories form the target mode at the end of the PhC waveguide.[212] The total length of the device is less than 10 µm. Low-crosstalk and broadband Y-junction MDM (de)multiplexers are utilized in a 40-Gb s^{-1} non-return-to-zero on-off keying (NRZ-OOK) signal transmission.[213] Aggregate bandwidths of 20 and 60 Gb s^{-1} for MDM and MDM-WDM on-chip links are also demonstrated with asymmetric Y junctions.[214] Mode conversion devices based on beam shaping have the merits of low IL and crosstalk. However, long branching waveguides are indispensable in these designs and the mode orders are limited by the number of branches one can handle at the same time.

Mode conversion based on constructive interference of coherent scattering was first implemented in MMI couplers with conversion lengths of several hundred microns.[215] The length was shortened to tens of microns by using SWG MMIs and the bandwidth reached 300 nm (1.4–1.7 µm).[216] Low-loss and fabrication tolerant mode converters was proposed using the MMI in exotic taper structures, which can be fabricated on the SOI platform with one-step etching.[217] 1 × 4 Y junctions and 4 × 4 MMI couplers were combined to realize arbitrary TE_0/TE_1/TE_2/TE_3 mode conversions in a single device.[218] However, similar to the mode converters based on the branching

© 2020 WILEY-VCH Verlag GmbH & Co. KGaA, Weinheim

Table 8. Comparison of the performances of mode conversion devices.

Structure and reference	Mode order	Size [µm × µm]	IL [dB]	Crosstalk [dB]	Bandwidth [nm]
Mode (de)multiplexer using shortcuts to adiabaticity[199]	TE_0-to-TE_3 (Experiment)	2.5 × 150	<1.3	<–23	100
Mode (de)multiplexer based on SWG[204]	TE_0-to-TE_{10} (Experiment)	4.2 × 5	<2.3	<–19.8	50
Adiabatic DC based on SWG[205]	TE_0-to-TE_{12} (Experiment)	5 × 75	<1.5	NA	75
SWG MMI[216]	TE_0-to-TE_1 (Theory)	36 × 3.7	<0.84	<–20	300
Nanostructure based on inverse design[221]	TE_0-to-TE_3 (Theory)	1.6 × 2.4	<0.43	NA	NA
Waveguide with metasurface[225]	TE_0-to-TE_2 (Experiment)	1.4 × 6.736	<1	<–10	20
Waveguide with polygonal slot[226]	TE_0-to-TE_2 (Theory)	2 × 8	<0.03	<–26.4	100

waveguides, the number of channels is restricted by the number of output ports in the MMI coupler. Other schemes based on programmed structures in waveguides were also proposed to achieve conversion lengths of only a few microns in the mode converters, including defects in the PhC waveguide[219,220] and computer-generated nanostructures based on inverse design algorithms.[221] Although these devices are the most compact reported thus far, the ultrafine structures usually demand fabrication techniques with extreme accuracy, which makes them less attractive in real applications.

The gradient phase can be introduced by metasurfaces or metamarials to assist the mode conversion in dielectric waveguides. For example, etching patterns were designed using the effective medium theory to realize 20-µm long mode converters in silicon waveguides.[222] The TE_0-to-TE_1 mode converter was experimentally demonstrated in an SOI waveguide, with a total length of 23 µm, high mode purity, and relatively low IL.[223] Gradient metasurface structures consisting of phased arrays of plasmonic or dielectric nanoantennas were applied at subwavelength intervals to realize waveguide mode converters of ≈10 µm on silicon, silicon nitride, and lithium niobite platforms.[224] TE_0-to-TE_1 and TE_0-to-TE_2 mode converters were proposed and experimentally demonstrated using all-dielectric metasurface structures with tilted subwavelength slots.[225] The coupling lengths are 5.75 and 6.736 µm for the TE_0-to-TE_1 and TE_0-to-TE_2 mode conversion, respectively. Similar mode-order converters based on polygonal slots have been studied by simulations.[226] Mode converters based on this principle are ultra-compact, broadband, and fabrication-tolerant. Since it is a burgeoning technique and shows potential in realizing high-quality mode conversion, the topic is attracting research attention.

Mode conversion devices with state-of-the-art performances are summarized in **Table 8**. Employing adiabaticity and SWGs in the design of mode converters shows potential for broadening the working bandwidth of the device, while introducing metasurfaces into the mode converter design is promising for shortening the device length and reducing the IL and crosstalk.

5.4. Graphene–Silicon Hybrid Devices

Since graphene has a high thermal conductivity as well as a relatively low absorption rate compared with metal heaters, graphene can directly contact the silicon waveguide as an ideal micro-heater, and the loss of such a graphene–silicon hybrid waveguide is relatively low with a proper length of the graphene heater. This is in contrast with traditional metal microheaters in the CMOS process, in which a buffer silicon oxide layer is always introduced between the metal layer and the waveguide layer in order to reduce the loss from the metal. Thus, the response time can be reduced and the heating efficiency can be increased.

For a graphene-based tunable TO device, electrical power can be applied onto the graphene layer, which can function as a resistor. The graphene layer can then absorb electrical power and heat the waveguide underneath. **Figure 12** shows the 2D temperature distribution for a graphene–silicon hybrid structure. In our simulation, the thermal conductivities of graphene, silicon, and silicon oxide were set to ≈2000, ≈80, and ≈1.38 W m^{-1} K^{-1}, respectively. The heat convection coefficient of the air was ≈5 W m^{-2} K^{-1}.[101] The temperature of the silicon waveguide increased by approximately 5.8 K if the thermal energy density (Q) in the graphene layer was set to 30×10^{15} W m^{-3}. As the TO coefficient of silicon is $\mathrm{d}n/\mathrm{d}T = 1.8 \times 10^{-4}$ K^{-1}, the effective index of the silicon-graphene hybrid waveguide (n_{eff}) can thus increase. The real part of n_{eff} affects the phase delay of the waveguide, while the imaginary part determines the loss.

Based on the aforementioned scheme, various graphene–silicon hybrid waveguide-based TO devices have been demonstrated (see **Table 9**), including optical switches/modulators and optical filters. A highly efficient TO microring modulator assisted by graphene[227] was implemented with a heating efficiency of 0.104 nm mW^{-1}. To enhance the heating efficiency, a tunable silicon photonic microdisk resonator with a transparent graphene nanoheater was demonstrated. The diameter of this micro-disk can be reduced to 2 µm to tightly confine the optical

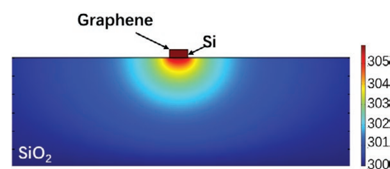

Figure 12. 2D temperature distribution of the hybrid graphene–silicon waveguide. The dimensions of the silicon waveguide are 500 nm × 220 nm. The thickness of graphene was set to 0.5 nm and H_s is 0 nm.

© 2020 WILEY-VCH Verlag GmbH & Co. KGaA, Weinheim

Table 9. Recent progress of graphene–silicon TO devices.

Structure and reference	Tuning efficiency [nm mW^{-1}]	Response time [µs]	Spacer
Graphene on micro-ring[227]	0.104	0.75	No
Graphene on micro-disk[30]	1.67	12.8	No
Graphene on PhC[37]	1.07	0.75	No
Graphene on nanobeam[101]	1.5	1.47	No
Graphene on micro-ring[228]	0.33	3	Yes

mode volume. By integrating a graphene micro-heater on the device, the efficiency is enhanced to 1.67 nm mW^{-1}.[30] The slow light effect can also be utilized to improve the tuning efficiency. By using a silicon PhC waveguide and an added layer of the graphene micro-heater,[37] a tuning efficiency of 1.07 nm mW^{-1} was obtained. Based on a 1D PhC cavity with an ultrasmall mode volume, a tuning efficiency of 1.5 nm mW^{-1} was demonstrated in the experiment.[101] Owing to the high thermal conductivity of graphene, the rise/fall time constants for graphene-based TO devices are approximately 1 µs, which are much faster than those of metal heater-based TO devices.

Based on the aforementioned experimental results, the efficiency can be increased by using an ultra-small mode volume resonator and then enhancing the light–matter interaction between the graphene and optical light. However, the loss from graphene can absorb light power and thus still strongly affect the Q factor and the ER. Thus, to resolve this issue, the graphene heater can be located at a distance of 240 nm from the waveguide,[228] so light absorption can be eliminated. In that work, HSQ was used as the spacer material between the graphene and waveguide. The tuning efficiency is 0.33 nm mW^{-1}, while the response time is ≈3 µs. Table 9 summarizes some recent results.

6. Conclusion and Perspective

This paper reviews the rapidly growing silicon photonics technologies, covering material properties, fabrication processes, and relevant applications. Starting from the materials, silicon, Si_3N_4, silica, and graphene on silicon were introduced. The optical properties of the waveguides built on the aforementioned materials were then discussed, and the corresponding fabrication processes were illustrated. The fabrication of passive waveguide devices, and their device structures, principles, and performances were reviewed. These devices are divided into fixed and tunable filters; polarization beam splitters and rotators; mode conversion and multiplexing devices; and graphene-on-silicon devices. These passive silicon photonic waveguide devices are essential building blocks for high density photonic circuits. Future challenges may lie in practical issues in mass production of large scale circuits, such as scalability limited by the waveguide loss, and repeatability in the fabrication and therefore the yield of the components. One important consideration is the co-integration with active components including lasers, modulators, and detectors. Light emission, modulation and detection are indispensable functions, which are enabled by these active devices. While significant progress has been made on silicon modulators and GeSi photo detectors, the laser source remains a challenge as the Si material does not show direct bandgap for light emission. Hybrid integration is therefore of particular interest, in the form of growing III-V materials on silicon or through bonding of two chips with different materials. Hybrid integration not only is needed for laser sources, but also shows advantages in other scenarios such as modulation and nonlinear processing by combining suitable materials of excellent properties for particular applications. For example, LiN_bO_3 has enabled ultra-high-speed modulation on silicon. A more detailed perspective on hybrid photonics beyond silicon can be found in ref. [229]. In summary, silicon photonic waveguide devices play increasingly important roles in a wide range of applications, including but not limited to communications, computing, sensing, quantum information processing, biology, and energy.

Acknowledgements

This article is part of the Advanced Materials Technologies Hall of Fame article series, which recognizes the excellent contributions of leading researchers to the field of technology-related materials science. This work was supported in part by the National Key R&D Program of China under grant 2019YFB1803602 and the National Natural Science Foundation of China (NSFC) (61835008, 61860206001). The authors thank the Center for Advanced Electronic Materials and Devices (AEMD) of Shanghai Jiao Tong University (SJTU) for their support in device fabrication. The authors would like to acknowledge the helpful comments from Yu He and Hongwei Wang.

Conflict of Interest

The authors declare no conflict of interest.

Keywords

fabrication, integrated devices, silicon photonics, waveguide

Received: December 30, 2019
Revised: April 15, 2020
Published online:

[1] R. Soref, *IEEE J. Sel. Top. Quantum Electron.* **2006**, *12*, 1678.
[2] T. Hu, B. Dong, X. Luo, T.-Y. Liow, J. Song, C. Lee, G.-Q. Lo, *Photonics Research* **2017**, *5*, 417.
[3] E. D. Palik, *Handbook of Optical Constants of Solids*, Academic, New York **1998**.
[4] T. D. Bucio, C. Lacava, M. Clementi, J. Faneca, I. Skandalos, A. Baldycheva, M. Galli, K. Debnath, P. Petropoulos, F. Gardes, *IEEE J. Sel. Top. Quantum Electron.* **2020**, *26*, 1.
[5] T. Miya, *IEEE J. Sel. Top. Quantum Electron.* **2000**, *6*, 38.
[6] Y. Zhang, Y. He, Q. Zhu, X. Guo, C. Qiu, Y. Su, R. Soref, *Opt. Lett.* **2018**, *43*, 4518.
[7] Q. Fang, J. F. Song, T. Y. Liow, H. Cai, M. B. Yu, G. Q. Lo, D. L. Kwong, *IEEE Photonics Technol. Lett.* **2011**, *23*, 525.

 © 2020 WILEY-VCH Verlag GmbH & Co. KGaA, Weinheim

[8] D. J. Moss, R. Morandotti, A. L. Gaeta, M. Lipson, *Nat. Photonics* **2013**, *7*, 597.
[9] S. Miller, K. Luke, Y. Okawachi, J. Cardenas, A. L. Gaeta, M. Lipson, *Opt. Express* **2014**, *22*, 26517.
[10] M. Li, H. X. Tang, *Nat. Mater.* **2019**, *18*, 9.
[11] P. E. Barclay, K. Srinivasan, O. Painter, *Opt. Express* **2005**, *13*, 801.
[12] A. Arbabi, L. L. Goddard, *Opt. Lett.* **2013**, *38*, 3878.
[13] K. Ikeda, R. E. Saperstein, N. Alic, Y. Fainman, *Opt. Express* **2008**, *16*, 12987.
[14] A. Boskovic, S. V. Chernikov, J. R. Taylor, L. Gruner-Nielsen, O. A. Levring, *Opt. Lett.* **1996**, *21*, 1966.
[15] Z. P. Sun, A. Martinez, F. Wang, *Nat. Photonics* **2016**, *10*, 227.
[16] M. Liu, X. B. Yin, E. Ulin-Avila, B. S. Geng, T. Zentgraf, L. Ju, F. Wang, X. Zhang, *Nature* **2011**, *474*, 64.
[17] X. T. Gan, R. J. Shiue, Y. D. Gao, I. Meric, T. F. Heinz, K. Shepard, J. Hone, S. Assefa, D. Englund, *Nat. Photonics* **2013**, *7*, 883.
[18] X. M. Wang, Z. Z. Cheng, K. Xu, H. K. Tsang, J. B. Xu, *Nat. Photonics* **2013**, *7*, 888.
[19] H. T. Yuan, X. G. Liu, F. Afshinmanesh, W. Li, G. Xu, J. Sun, B. Lian, A. G. Curto, G. J. Ye, Y. Hikita, Z. X. Shen, S. C. Zhang, X. H. Chen, M. Brongersma, H. Y. Hwang, Y. Cui, *Nat. Nanotechnol.* **2015**, *10*, 707.
[20] L. K. Li, F. Y. Yang, G. J. Ye, Z. C. Zhang, Z. W. Zhu, W. K. Lou, X. Y. Zhou, L. Li, K. Watanabe, T. Taniguchi, K. Chang, Y. Y. Wang, X. H. Chen, Y. B. Zhang, *Nat. Nanotech.* **2016**, *11*, 592.
[21] Y. Chen, G. B. Jiang, S. Q. Chen, Z. N. Guo, X. F. Yu, C. J. Zhao, H. Zhang, Q. L. Bao, S. C. Wen, D. Y. Tang, D. Y. Fan, *Opt. Express* **2015**, *23*, 12823.
[22] C. Y. Tang, P. K. Cheng, L. Tao, H. Long, L. H. Zeng, Q. Wen, Y. H. Tsang, *J. Lightwave Technol.* **2017**, *35*, 4120.
[23] M. W. Iqbal, M. Z. Iqbal, M. F. Khan, M. A. Shehzad, Y. Seo, J. H. Park, C. Hwang, J. Eom, *Sci. Rep.* **2015**, *5*, 10699.
[24] L. H. Zeng, L. L. Tao, C. Y. Tang, B. Zhou, H. Long, Y. Chai, S. P. Lau, Y. H. Tsang, *Sci. Rep.* **2016**, *6*, 20343.
[25] C. H. Liu, Y. C. Chang, T. B. Norris, Z. H. Zhong, *Nat. Nanotechnol.* **2014**, *9*, 273.
[26] H. Cai, Y. H. Cheng, H. Zhang, Q. Z. Huang, J. S. Xia, R. Barille, Y. Wang, *Opt. Express* **2016**, *24*, 24105.
[27] H. Lu, X. T. Gan, D. Mao, J. L. Zhao, *Photonics Research* **2017**, *5*, 162.
[28] H. Lu, X. T. Gan, B. H. Jia, D. Mao, J. L. Zhao, *Opt. Lett.* **2016**, *41*, 4743.
[29] R. Hao, J. Y. Jiao, X. L. Peng, Z. Zhen, R. Dagarbek, Y. J. Zou, E. Li, *Opt. Lett.* **2019**, *44*, 2586.
[30] L. H. Yu, Y. L. Yin, Y. C. Shi, D. X. Dai, S. L. He, *Optica* **2016**, *3*, 159.
[31] Y. X. Yang, Z. Z. Xu, X. H. Jiang, Y. He, X. H. Guo, Y. Zhang, C. Y. Qiu, Y. K. Su, *Photonics Research* **2018**, *6*, 965.
[32] A. Majumdar, J. Kim, J. Vuckovic, F. Wang, *Nano Lett.* **2013**, *13*, 515.
[33] Y. H. Ding, X. L. Zhu, S. S. Xiao, H. Hu, L. H. Frandsen, N. A. Mortensen, K. Yvind, *Nano Lett.* **2015**, *15*, 4393.
[34] C. T. Phare, Y. H. D. Lee, J. Cardenas, M. Lipson, *Nat. Photonics* **2015**, *9*, 511.
[35] M. Liu, X. B. Yin, X. Zhang, *Nano Lett.* **2012**, *12*, 1482.
[36] T. Mueller, F. N. A. Xia, P. Avouris, *Nat. Photonics* **2010**, *4*, 297.
[37] S. Q. Yan, X. L. Zhu, L. H. Frandsen, S. S. Xiao, N. A. Mortensen, J. J. Dong, Y. H. Ding, *Nat. Commun.* **2017**, *8*, 14411.
[38] T. Gu, N. Petrone, J. F. McMillan, A. van der Zande, M. Yu, G. Q. Lo, D. L. Kwong, J. Hone, C. W. Wong, *Nat. Photonics* **2012**, *6*, 554.
[39] W. Li, B. G. Chen, C. Meng, W. Fang, Y. Xiao, X. Y. Li, Z. F. Hu, Y. X. Xu, L. M. Tong, H. Q. Wang, W. T. Liu, J. M. Bao, Y. R. Shen, *Nano Lett.* **2014**, *14*, 955.
[40] S. L. Yu, X. Q. Wu, K. R. Chen, B. G. Chen, X. Guo, D. X. Dai, L. M. Tong, W. T. Liu, Y. R. Shen, *Optica* **2016**, *3*, 541.
[41] R. A. Soref, J. Schmidtchen, K. Petermann, *IEEE J. Quantum Electron.* **1991**, *27*, 1971.
[42] I. Giuntoni, D. Stolarek, D. I. Kroushkov, J. Bruns, L. Zimmermann, B. Tillack, K. Petermann, *Opt. Express* **2012**, *20*, 11241.
[43] D. Dai, S. He, *Journal of the Optical Society of America A* **2004**, *21*, 113.
[44] Q. Xu, D. Fattal, R. G. Beausoleil, *Opt. Express* **2008**, *16*, 4309.
[45] Y. Zhang, Y. He, X. Jiang, B. Liu, C. Qiu, Y. Su, R. A. Soref, *APL Photonics.* **2016**, *1*, 091304.
[46] F. P. Payne, J. P. R. Lacey, *Optical and Quantum Electronics* **1994**, *26*, 977.
[47] R. Baets, A. Z. Subramanian, S. Clemmen, B. Kuyken, P. Bienstman, N. Le Thomas, G. Roelkens, D. Van Thourhout, P. Helin, S. Severi, presented at OFC, Anaheim, CA, March, **2016**.
[48] K. Debnath, H. Arimoto, M. K. Husain, A. Prasmusinto, A. Al-Attili, R. Petra, H. M. H. Chong, G. T. Reed, S. Saito, *Front. Mater.* **2016**, *3*, 10.
[49] T. Horikawa, D. Shimura, T. Mogami, *MRS Commun.* **2016**, *6*, 9.
[50] C. Bellegarde, E. Pargon, C. Sciancalepore, C. Petit-Etienne, V. Hugues, D. Robin-Brosse, J. Hartmann, P. Lyan, *IEEE Photonics Technol. Lett.* **2018**, *30*, 591.
[51] F. Xia, L. Sekaric, Y. Vlasov, *Nat. Photonics* **2007**, *1*, 65.
[52] M. Gnan, S. Thoms, D. S. Macintyre, R. M. D. L. Rue, M. Sorel, *Electron. Lett.* **2008**, *44*, 115.
[53] Y. A. Vlasov, S. J. McNab, *Opt. Express* **2004**, *12*, 1622.
[54] W. Bogaerts, R. Baets, P. Dumon, V. Wiaux, S. Beckx, D. Taillaert, B. Luyssaert, J. V. Campenhout, P. Bienstman, D. V. Thourhout, *J. Lightwave Technol.* **2005**, *23*, 401.
[55] D. Shimura, T. Horikawa, H. Okayama, S. Jeong, M. Tokushima, H. Sasaki, T. Mogami, presented at GFP, Paris, France, August **2014**.
[56] P. Dong, W. Qian, H. Liang, R. Shafiiha, D. Feng, G. Li, J. E. Cunningham, A. V. Krishnamoorthy, M. Asghari, *Opt. Express* **2010**, *18*, 20298.
[57] R. Halir, P. J. Bock, P. Cheben, A. Ortega-Moñux, C. Alonso-Ramos, J. H. Schmid, J. Lapointe, D. X. Xu, J. G. Wangüemert-Pérez, Í. Molina-Fernández, *Laser Photonics Rev.* **2015**, *9*, 25.
[58] D. Dai, C. Li, S. Wang, H. Wu, Y. Shi, Z. Wu, S. Gao, T. Dai, H. Yu, H.-K. Tsang, *Laser Photonics Rev.* **2018**, *12*, 1700109.
[59] J. F. Bauters, M. J. R. Heck, D. John, D. Dai, M.-C. Tien, J. S. Barton, A. Leinse, R. G. Heideman, D. J. Blumenthal, J. E. Bowers, *Opt. Express* **2011**, *19*, 3163.
[60] J. F. Bauters, M. J. R. Heck, D. D. John, J. S. Barton, C. M. Bruinink, A. Leinse, R. G. Heideman, D. J. Blumenthal, J. E. Bowers, *Opt. Express* **2011**, *19*, 24090.
[61] K. Shang, S. Pathak, B. Guan, G. Liu, S. J. B. Yoo, *Opt. Express* **2015**, *23*, 21334.
[62] J. P. Epping, M. Hoekman, R. Mateman, A. Leinse, R. G. Heideman, A. van Rees, P. J. M. van der Slot, C. J. Lee, K.-J. Boller, *Opt. Express* **2015**, *23*, 642.
[63] K. Luke, A. Dutt, C. B. Poitras, M. Lipson, *Opt. Express* **2013**, *21*, 22829.
[64] M. Melchiorri, N. Daldosso, F. Sbrana, L. Pavesi, G. Pucker, C. Kompocholis, P. Bellutti, A. Lui, *Appl. Phys. Lett.* **2005**, *86*, 121111.
[65] M. J. Shaw, J. Guo, G. A. Vawter, S. Habermehl, C. T. Sullivan, presented at SPIE, San Jose, CA, United States, January **2005**.
[66] K. Worhoff, E. Klein, G. Hussein, A. Driessen, presented at International Conference on Transparent Optical Networks, Athens, Greece, June **2008**.
[67] A. Z. Subramanian, P. Neutens, A. Dhakal, R. Jansen, T. Claes, X. Rottenberg, F. Peyskens, S. Selvaraja, P. Helin, B. D. Bois, K. Leyssens, S. Severi, P. Deshpande, R. Baets, P. V. Dorpe, *IEEE Photonics Journal* **2013**, *5*, 2202809.
[68] S. Romero-García, F. Merget, F. Zhong, H. Finkelstein, J. Witzens, *Opt. Express* **2013**, *21*, 14036.

 © 2020 WILEY-VCH Verlag GmbH & Co. KGaA, Weinheim

[69] P. T. Lin, V. Singh, H.-Y. G. Lin, T. Tiwald, L. C. Kimerling, A. M. Agarwal, *Adv. Opt. Mater.* **2013**, *1*, 732.
[70] Y. Huang, J. Song, X. Luo, T.-Y. Liow, G.-Q. Lo, *Opt. Express* **2014**, *22*, 21859.
[71] K. Luke, Y. Okawachi, M. R. E. Lamont, A. L. Gaeta, M. Lipson, *Opt. Lett.* **2015**, *40*, 4823.
[72] M. Pfeiffer, A. Kordts, V. Brasch, M. Zervas, M. Geiselmann, J. Jost, T. Kippenberg, *Optica* **2016**, *3*, 20.
[73] X. Ji, F. A. S. Barbosa, S. P. Roberts, A. Dutt, J. Cardenas, Y. Okawachi, A. Bryant, A. L. Gaeta, M. Lipson, *Optica* **2017**, *4*, 619.
[74] S. S. Saseendran, T. D. Kongnyuy, B. Figeys, F. Buja, B. Troia, S. Kerman, A. Marinins, R. Jansen, X. Rottenberg, D. S. Tezcan, P. Soussan, presented at OFC, Anaheim, CA, March **2019**.
[75] X. Ji, X. Yao, Y. Gan, A. Mohanty, M. A. Tadayon, C. P. Hendon, M. Lipson, *APL Photonics.* **2019**, *4*, 090803.
[76] A. Himeno, K. Kato, T. Miya, *IEEE J. Sel. Top. Quantum Electron.* **1998**, *4*, 913.
[77] M. R. Poulsen, P. I. Borel, J. Fage-Pedersen, J. Huebner, M. Kristensen, J. H. Povlsen, K. Rottwitt, M. Svalgaard, W. Svendsen, *Optical Engineering* **2003**, *42*, 2821.
[78] Y. Hida, Y. Hibino, H. Okazaki, Y. Ohmori, presented at IPR, Dana Point, CA, February **1995**.
[79] M. Yanagisawa, Y. Inoue, M. Ishii, T. Oguchi, Y. Hida, H. Izumita, N. Araki, T. Sugie, presented at OFC, Los Angeles, CA, February **2004**.
[80] Y. Hibino, *IEEE J. Sel. Top. Quantum Electron.* **2002**, *8*, 1090.
[81] J. Kim, H. Son, D. J. Cho, B. S. Geng, W. Regan, S. F. Shi, K. Kim, A. Zettl, Y. R. Shen, F. Wang, *Nano Lett.* **2012**, *12*, 5598.
[82] C. Y. Qiu, W. L. Gao, R. Vajtai, P. M. Ajayan, J. Kono, Q. F. Xu, *Nano Lett.* **2014**, *14*, 6811.
[83] X. Yin, X. M. Ke, L. Chen, T. Zhang, J. H. Li, Z. S. Zhu, X. Li, *J. Lightwave Technol.* **2016**, *34*, 3181.
[84] C. Y. Pei, L. Z. Yang, G. C. Wang, Y. H. Wang, X. Q. Jiang, Y. L. Hao, Y. B. Li, J. Y. Yang, *IEEE Photonics Technol. Lett.* **2015**, *27*, 927.
[85] Q. L. Bao, H. Zhang, B. Wang, Z. H. Ni, C. H. Y. X. Lim, Y. Wang, D. Y. Tang, K. P. Loh, *Nat. Photonics* **2011**, *5*, 411.
[86] F. Bœuf, J. F. Carpentier, C. Baudot, P. Le Maitre, J.-R. Manouvrier, *Silicon Photonics III: Systems and Applications*, Springer Berlin Heidelberg, Berlin, Heidelberg **2016**, p. 277.
[87] A. E. Lim, J. Song, Q. Fang, C. Li, X. Tu, N. Duan, K. K. Chen, R. P. Tern, T. Liow, *IEEE J. Sel. Top. Quantum Electron.* **2014**, *20*, 405.
[88] R. J. Bojko, J. Li, L. He, T. Baehr-Jones, M. Hochberg, Y. Aida, *J. Vac. Sci. Technol., B: Nanotechnol. Microelectron.: Mater., Process., Meas., Phenom.* **2011**, *29*, 06F309.
[89] A. E.-J. Lim, T.-Y. Liow, J.-F. Song, M.-B. Yu, C. Li, X.-G. Tu, K.-K. Chen, R. P.-C. Tern, Y. Huang, X.-S. Luo, G.-Q. Lo, *Silicon Photonics III: Systems and Applications*, Springer Berlin Heidelberg, Berlin, Heidelberg **2016**, p. 191.
[90] R. Heideman, A. Leinse, W. Hoving, R. Dekker, D. Geuzebroek, E. Klein, R. Stoffer, C. Roeloffzen, L. Zhuang, A. Meijerink, presented at SPIE, San Jose, CA, United States, February **2009**.
[91] A. Novack, M. Streshinsky, R. Ding, Y. Liu, E.-J. Lim Andy, G.-Q. Lo, T. Baehr-Jones, M. Hochberg, *Nanophotonics* **2014**, *3*, 205.
[92] F. Ay, A. Aydinli, *Optical Materials* **2004**, *26*, 33.
[93] F. Karouta, K. Vora, J. Tian, C. Jagadish, *J. Phys. D: Appl. Phys.* **2012**, *45*, 445301.
[94] S. Bhaviripudi, X. T. Jia, M. S. Dresselhaus, J. Kong, *Nano Lett.* **2010**, *10*, 4128.
[95] L. J. Shi, R. R. Wang, H. T. Zhai, Y. Q. Liu, L. Gao, J. Sun, *Phys. Chem. Chem. Phys.* **2015**, *17*, 4231.
[96] M. Asghari, A. V. Krishnamoorthy, *Nat. Photonics* **2011**, *5*, 268.
[97] J. Wang, H. Shen, L. Fan, R. Wu, B. Niu, L. T. Varghese, Y. Xuan, D. E. Leaird, X. Wang, F. Gan, A. M. Weiner, M. Qi, *Nat. Commun.* **2015**, *6*, 5957.
[98] L. Gu, W. Jiang, X. Chen, R. T. Chen, *IEEE Photonics Technol. Lett.* **2007**, *19*, 342.
[99] Q. Li, D. Nikolova, D. M. Calhoun, Y. Liu, R. Ding, T. Baehr-Jones, M. Hochberg, K. Bergman, *IEEE Photonics Technol. Lett.* **2015**, *27*, 1981.
[100] T. Yamane, N. Nagai, S.-i. Katayama, M. Todoki, *J. Appl. Phys.* **2002**, *91*, 9772.
[101] Z. Z. Xu, C. Y. Qiu, Y. X. Yang, Q. M. Zhu, X. H. Jiang, Y. Zhang, W. L. Gao, Y. K. Su, *Opt. Express* **2017**, *25*, 19479.
[102] Y. Yanagase, S. Suzuki, Y. Kokubun, C. Sai Tak, *J. Lightwave Technol.* **2002**, *20*, 1525.
[103] Q. Li, M. Soltani, S. Yegnanarayanan, A. Adibi, *Opt. Express* **2009**, *17*, 4.
[104] R. Boeck, J. Flueckiger, L. Chrostowski, N. A. F. Jaeger, *Opt. Express* **2013**, *21*, 9103.
[105] P. Dong, N.-N. Feng, D. Feng, W. Qian, H. Liang, D. C. Lee, B. J. Luff, T. Banwell, A. Agarwal, P. Toliver, R. Menendez, T. K. Woodward, M. Asghari, *Opt. Express* **2010**, *18*, 23.
[106] J. B. K. P. A. Morton, Z. Mizrahi, S. J. Morton, presented at CLEO, San Jose, CA, USA, **2014**.
[107] F. Horst, W. M. J. Green, S. Assefa, S. M. Shank, Y. A. Vlasov, B. J. Offrein, *Opt. Express* **2013**, *21*, 11652.
[108] M. Kuznetsov, *J. Lightwave Technol.* **1994**, *12*, 2.
[109] Q. Deng, L. Liu, R. Zhang, X. Li, J. Michel, Z. Zhou, *Opt. Express* **2016**, *24*, 26.
[110] Y. Zhao, X. Wang, D. Gao, J. Dong, X. Zhang, *Frontiers of Optoelectronics* **2019**, *12*, 148.
[111] S. Liao, Y. Ding, J. Dong, T. Yang, X. Chen, D. Gao, X. Zhang, *Opt. Express* **2015**, *23*, 9.
[112] S. Liao, Y. Ding, J. Dong, S. Yan, X. Wang, X. Zhang, *Opt. Express* **2016**, *24*, 21.
[113] S. Liao, Y. Ding, C. Peucheret, T. Yang, J. Dong, X. Zhang, *Opt. Express* **2014**, *22*, 26.
[114] D. Charron, J. St-Yves, O. Jafari, S. LaRochelle, W. Shi, *Opt. Lett.* **2018**, *43*, 895.
[115] B. Liu, Y. Zhang, Y. He, X. Jiang, J. Peng, C. Qiu, Y. Su, *Opt. Express* **2017**, *25*, 10.
[116] H. Yun, M. Hammood, S. Lin, L. Chrostowski, N. A. F. Jaeger, *Opt. Lett.* **2019**, *44*, 20.
[117] R. Xiao, Y. Shi, Y. Zhao, X. Chen, presented at OFC, San Diego, CA, United States, March **2018**.
[118] L. Zhu, J. Sun, Y. Zhou, *Opt. Express* **2019**, *27*, 16.
[119] S. Pathak, D. Van Thourhout, W. Bogaerts, *Opt. Lett.* **2013**, *38*, 2961.
[120] S. Chen, Y. Shi, S. He, D. Dai, *IEEE Photon. Technol. Lett.* **2016**, *28*, 17.
[121] K. Okamoto, *IEEE J. Sel. Top. Quantum Electron.* **2014**, *20*, 248.
[122] P. Cheben, J. H. Schmid, A. Delâge, A. Densmore, S. Janz, B. Lamontagne, J. Lapointe, E. Post, P. Waldron, D. X. Xu, *Opt. Express* **2007**, *15*, 2299.
[123] S. T. S. Cheung, B. Guan, S. S. Djordjevic, K. Okamoto, S. J. B. Yoo, presented at CLEO, San Jose, California, May **2012**.
[124] S. Cheung, T. Su, K. Okamoto, S. J. B. Yoo, *IEEE J. Sel. Top. Quantum Electron.* **2014**, *20*, 310.
[125] S. Chen, X. Fu, J. Wang, Y. Shi, S. He, D. Dai, *J. Lightwave Technol.* **2015**, *33*, 11.
[126] Q. Yu, Z. Pan, L.-S. Yan, A. E. Willner, *J. Lightwave Technol.* **2002**, *20*, 12.
[127] J. Yao, M. C. Wu, *Opt. Lett.* **2009**, *34*, 17.
[128] L. Chen, N. Sherwood-Droz, M. Lipson, *Opt. Lett.* **2007**, *32*, 22.
[129] T. Dai, A. Shen, G. Wang, Y. Wang, Y. Li, X. Jiang, J. Yang, *Opt. Lett.* **2016**, *41*, 20.
[130] J. R. Ong, R. Kumar, S. Mookherjea, *IEEE Photon. Technol. Lett.* **2013**, *25*, 16.
[131] H. Wang, J. Dai, H. Jia, S. Shao, X. Fu, L. Zhang, L. Yang, *Nanophotnics.* **2018**, *7*, 8.

© 2020 WILEY-VCH Verlag GmbH & Co. KGaA, Weinheim

[132] G. Poulopoulos, G. Giannoulis, N. Iliadis, D. Kalavrouziotis, D. Apostolopoulos, H. Avramopoulos, *J. Lightwave Technol.* **2019**, *37*, 300.
[133] X. Deng, L. Yan, H. Jiang, X. Feng, W. Pan, B. Luo, *IEEE Photon. J.* **2018**, *10*, 3.
[134] Y. Ding, M. Pu, L. Liu, J. Xu, C. Peucheret, X. Zhang, D. Huang, H. Ou, *Opt. Express* **2011**, *19*, 7.
[135] P. Orlandi, F. Morichetti, M. J. Strain, M. Sorel, P. Bassi, A. Melloni, *J. Lightwave Technol.* **2014**, *32*, 897.
[136] J. St-Yves, H. Bahrami, P. Jean, S. LaRochelle, W. Shi, *Opt. Lett.* **2015**, *40*, 5471.
[137] J. Jiang, H. Qiu, G. Wang, Y. Li, T. Dai, X. Wang, H. Yu, J. Yang, X. Jiang, *Opt. Express* **2018**, *26*, 1.
[138] P. Orlandi, C. Ferrari, M. J. Strain, A. Canciamilla, F. Morichetti, M. Sorel, P. Bassi, A. Melloni, *Opt. Lett.* **2012**, *37*, 3669.
[139] F. Gan, T. Barwicz, M. A. Popovic, M. S. Dahlem, C. W. Holzwarth, P. T. Rakich, H. I. Smith, E. P. Ippen, F. X. Kartner, presented at Photonics in Switching, San Francisco, CA, United States, August **2007**.
[140] J. Zhang, S. He, *Opt. Express* **2017**, *25*, 11.
[141] M. R. Watts, W. A. Zortman, D. C. Trotter, G. N. Nielson, D. L. Luck, R. W. Young, presented at CLEO, Baltimore, Maryland, United States, May **2009**.
[142] W. S. Fegadolli, N. Pavarelli, P. O'Brien, S. Njoroge, V. R. Almeida, A. Scherer, *ACS Photonics.* **2015**, *2*, 470.
[143] S. Yan, X. Zhu, L. H. Frandsen, S. Xiao, N. A. Mortensen, J. Dong, Y. Ding, *Nat. Commun.* **2017**, *8*, 1.
[144] P. Dong, W. Qian, H. Liang, R. Shafiiha, D. Feng, G. Li, J. E. Cunningham, A. V. Krishnamoorthy, M. Asghari, *Opt. Express* **2010**, *18*, 19.
[145] P. Dong, W. Qian, H. Liang, R. Shafiiha, N.-N. Feng, D. Feng, X. Zheng, A. V. Krishnamoorthy, M. Asghari, *Opt. Express* **2010**, *18*, 10.
[146] D. Dai, J. Bauters, J. E. Bowers, *Light: Sci. Appl.* **2012**, *1*, e1.
[147] M. R. Watts, H. A. Haus, E. P. Ippen, *Opt. Lett.* **2005**, *30*, 967.
[148] T. Barwicz, M. R. Watts, A. PopovicMilos, P. T. Rakich, L. Socci, F. X. Kartner, E. P. Ippen, H. I. Smith, *Nat. Photonics* **2007**, *1*, 57.
[149] D. Dai, *J. Lightwave Technol.* **2012**, *30*, 3281.
[150] Y. Kim, M. H. Lee, Y. Kim, K. H. Kim, *Opt. Lett.* **2018**, *43*, 3241.
[151] J. Feng, Z. Zhou, *Opt. Lett.* **2007**, *32*, 1662.
[152] Y. Zhang, Y. He, J. Wu, X. Jiang, R. Liu, C. Qiu, X. Jiang, J. Yang, C. Tremblay, Y. Su, *Opt. Express* **2016**, *24*, 6586.
[153] Y. Xu, J. Xiao, *Opt. Lett.* **2016**, *41*, 773.
[154] X. Sun, J. S. Aitchison, M. Mojahedi, *Opt. Express* **2017**, *25*, 8296.
[155] S. Gao, Y. Wang, K. Wang, E. Skafidas, *IEEE Photonics Technol. Lett.* **2016**, *28*, 1936.
[156] U. G. Yasa, M. Turduev, I. H. Giden, H. Kurt, *J. Lightwave Technol.* **2017**, *35*, 1677.
[157] H. Fukuda, K. Yamada, T. Tsuchizawa, T. Watanabe, H. Shinojima, S.-i. Itabashi, *Opt. Express* **2006**, *14*, 12401.
[158] D. Dai, L. Liu, S. Gao, D. X. Xu, S. He, *Laser Photonics Rev.* **2013**, *7*, 303.
[159] D. Dai, Z. Wang, J. E. Bowers, *Opt. Lett.* **2011**, *36*, 2590.
[160] M.-a. Komatsu, K. Saitoh, M. Koshiba, *Opt. Express* **2009**, *17*, 19225.
[161] Y. Tian, J. Qiu, C. Liu, S. Tian, Z. Huang, J. Wu, *Opt. Express* **2019**, *27*, 999.
[162] D. Dai, J. E. Bowers, *Opt. Express* **2011**, *19*, 18614.
[163] J. R. Ong, T. Y. L. Ang, E. Sahin, B. Pawlina, G. F. R. Chen, D. T. H. Tan, S. T. Lim, C. E. Png, *Opt. Lett.* **2017**, *42*, 4450.
[164] N. Zhao, C. Qiu, Y. He, Y. Zhang, Y. Su, *IEEE Photon. J.* **2019**, *11*, 1.
[165] J. Wang, D. Liang, Y. Tang, D. Dai, J. E. Bowers, *Opt. Lett.* **2013**, *38*, 4.
[166] Y. Zhang, Y. He, X. Jiang, B. Liu, C. Qiu, Y. Su, presented at GFP, Shanghai, China, August **2016**.
[167] H. Wu, Y. Tan, D. Dai, *Opt. Express* **2017**, *25*, 6069.
[168] P. Fu, T. Huang, K. Fan, D. Huang, *IEEE Photonics Journal* **2019**, *11*, 1.
[169] H. Qiu, Y. Su, P. Yu, T. Hu, J. Yang, X. Jiang, *Opt. Lett.* **2015**, *40*, 1885.
[170] Y. Zhang, Y. He, J. Wu, R. Liu, C. Qiu, Y. Su, presented at OFC, Anaheim, CA, March **2016**.
[171] H. Qiu, J. Jiang, P. Yu, J. Yang, H. Yu, X. Jiang, *Opt. Lett.* **2017**, *42*, 3912.
[172] P. Cheben, R. Halir, J. H. Schmid, H. A. Atwater, D. R. Smith, *Nature* **2018**, *560*, 565.
[173] Z. Guo, J. Xiao, *IEEE Photonics Technol. Lett.* **2017**, *29*, 1800.
[174] L. Xu, Y. Wang, A. Kumar, D. Patel, E. El-Fiky, Z. Xing, R. Li, D. V. Plant, *IEEE Photonics Technol. Lett.* **2018**, *30*, 403.
[175] C. Li, D. Dai, *Opt. Lett.* **2017**, *42*, 4243.
[176] B. Shen, P. Wang, R. Polson, R. Menon, *Nat. Photonics* **2015**, *9*, 378.
[177] H. Xu, D. Dai, Y. Shi, *Laser Photonics Rev.* **2019**, *13*, 1800349.
[178] A. Herrero-Bermello, J. M. Luque-González, A. V. Velasco, A. Ortega-Moñux, P. Cheben, R. Halir, *IEEE Photon. J.* **2019**, *11*, 1.
[179] D. Dai, J. E. Bowers, *Opt. Express* **2011**, *19*, 10940.
[180] K. Tan, Y. Huang, G.-Q. Lo, C. Lee, C. Yu, *Opt. Express* **2016**, *24*, 14506.
[181] Y. Ding, H. Ou, C. Peucheret, *Opt. Lett.* **2013**, *38*, 1227.
[182] J. Wang, B. Niu, Z. Sheng, A. Wu, W. Li, X. Wang, S. Zou, M. Qi, F. Gan, *Opt. Express* **2014**, *22*, 13565.
[183] H. Xu, Y. Shi, *Opt. Express* **2019**, *27*, 5588.
[184] M. Ma, A. H. K. Park, Y. Wang, H. Shoman, F. Zhang, N. A. F. Jaeger, L. Chrostowski, *Opt. Express* **2019**, *27*, 17581.
[185] G. Chen, L. Chen, W. Ding, F. Sun, R. Feng, *Opt. Lett.* **2013**, *38*, 1984.
[186] J. Zhang, M. Yu, G. Lo, D.-L. Kwong, presented at SPIE Photonics Europe, Brussels, Belgium, April **2010**.
[187] D. Chen, X. Xiao, L. Wang, W. Liu, Q. Yang, S. Yu, *Opt. Lett.* **2016**, *41*, 1070.
[188] H. Xu, Y. Shi, *Opt. Express* **2017**, *25*, 18485.
[189] J. Wang, B. Niu, Z. Sheng, A. Wu, X. Wang, S. Zou, M. Qi, F. Gan, *Opt. Express* **2014**, *22*, 4137.
[190] L. Liu, Y. Ding, K. Yvind, J. M. Hvam, *Opt. Express* **2011**, *19*, 12646.
[191] Y. Ding, L. Liu, C. Peucheret, H. Ou, *Opt. Express* **2012**, *20*, 20021.
[192] H. Guan, A. Novack, M. Streshinsky, R. Shi, Q. Fang, A. E.-J. Lim, G.-Q. Lo, T. Baehr-Jones, M. Hochberg, *Opt. Express* **2014**, *22*, 2489.
[193] K. Tan, Y. Huang, G.-Q. Lo, C. Yu, C. Lee, presented at OFC, Los Angeles, CA, March **2017**.
[194] Y. Zhang, Q. Zhu, Y. He, Y. Su, presented at OFC, San Diego, CA, March **2019**.
[195] Y. Xiong, J. G. Wangüemert-Pérez, D.-X. Xu, J. H. Schmid, P. Cheben, W. N. Ye, *Opt. Lett.* **2014**, *39*, 6931.
[196] Y. He, Y. Zhang, X. Wang, B. Liu, X. Jiang, C. Qiu, Y. Su, R. Soref, presented at OFC, Los Angeles, CA, March **2017**.
[197] D. Dai, Y. Tang, J. E. Bowers, *Opt. Express* **2012**, *20*, 13425.
[198] T. H. Pan, S. Y. Tseng, *Opt. Express* **2015**, *23*, 10405.
[199] D. Guo, T. Chu, *Opt. Express* **2017**, *25*, 9160.
[200] D. Dai, J. Wang, Y. Shi, *Opt. Lett.* **2013**, *38*, 1422.
[201] Y. Zhang, R. Zhang, Q. Zhu, Y. Yuan, Y. Su, *J. Lightwave Technol.* **2020**, *38*, 215.
[202] Y. D. Yang, Y. Li, Y. Z. Huang, A. W. Poon, *Opt. Express* **2014**, *22*, 22172.
[203] B. Stern, X. Zhu, C. P. Chen, L. D. Tzuang, J. Cardenas, K. Bergman, M. Lipson, *Optica* **2015**, *2*, 530.
[204] Y. He, Y. Zhang, Q. Zhu, S. An, R. Cao, X. Guo, C. Qiu, Y. Su, *J. Lightwave Technol.* **2018**, *36*, 5746.
[205] U. D. Dave, M. Lipson, presented at CLEO, San Jose, CA, United States, May **2019**.

 © 2020 WILEY-VCH Verlag GmbH & Co. KGaA, Weinheim

[206] S. Y. Tseng, M. C. Wu, *IEEE Photonics Technol. Lett.* **2010**, *22*, 1211.
[207] M. C. Wu, F. C. Hsiao, S. Y. Tseng, *IEEE Photon. Tech. Lett.* **2011**, *23*, 807.
[208] H. Qiu, H. Yu, T. Hu, G. Jiang, H. Shao, P. Yu, J. Yang, X. Jiang, *Opt. Express* **2013**, *21*, 17904.
[209] B. T. Lee, S. Y. Shin, *Opt. Lett.* **2003**, *28*, 1660.
[210] Y. Huang, G. Xu, S. T. Ho, *IEEE Photonics Technol. Lett.* **2006**, *18*, 2281.
[211] B. B. Oner, K. Ustun, H. Kurt, A. K. Okyay, G. Turhan-Sayan, *Opt. Express* **2015**, *23*, 3186.
[212] M. Turduev, B. B. Oner, I. H. Giden, H. Kurt, *J. Opt. Soc. Am. B* **2013**, *30*, 1569.
[213] C. Sun, Y. Yu, M. Ye, G. Chen, X. Zhang, *Sci. Rep.* **2016**, *6*, 38494.
[214] J. B. Driscoll, C. P. Chen, R. R. Grote, B. Souhan, J. I. Dadap, A. Stein, M. Lu, K. Bergman, R. M. Osgood, *Opt. Express* **2014**, *22*, 18543.
[215] J. Leuthold, J. Eckner, E. Gamper, P. A. Besse, H. Melchior, *J. Lightwave Technol.* **1998**, *16*, 1228.
[216] D. Gonzalez-Andrade, J. G. Wanguemert-Perez, A. V. Velasco, A. Ortega-Monux, A. Herrero-Bermello, I. Molina-Fernandez, R. Halir, P. Cheben, *IEEE Photonics Journal* **2018**, *10*, 1.
[217] D. Chen, X. Xiao, L. Wang, Y. Yu, W. Liu, Q. Yang, *Opt. Express* **2015**, *23*, 11152.
[218] H. D. T. Linh, T. C. Dung, K. Tanizawa, D. D. Thang, N. T. Hung, *IEEE J. Sel. Top. Quantum Electron.* **2020**, *26*, 1.
[219] G. Chen, J. U. Kang, *Opt. Lett.* **2005**, *30*, 1656.
[220] V. Liu, D. A. B. Miller, S. Fan, *Opt. Express* **2012**, *20*, 28388.
[221] J. Lu, J. Vuckovic, *Opt. Express* **2012**, *20*, 7221.
[222] D. Ohana, U. Levy, *Opt. Express* **2014**, *22*, 27617.
[223] D. Ohana, B. Desiatov, N. Mazurski, U. Levy, *Nano Lett.* **2016**, *16*, 7956.
[224] Z. Li, M. H. Kim, C. Wang, Z. Han, S. Shrestha, A. C. Overvig, M. Lu, A. Stein, A. M. Agarwal, M. Loncar, N. Yu, *Nat. Nanotechnol.* **2017**, *12*, 675.
[225] H. Wang, Y. Zhang, Y. He, Q. Zhu, L. Sun, Y. Su, *Adv. Opt. Mater.* **2019**, *7*, 1801191.
[226] L. Hao, R. Xiao, Y. Shi, P. Dai, Y. Zhao, S. Liu, J. Lu, X. Chen, *IEEE Photon. J.* **2019**, *11*, 6601210.
[227] S. Gan, C. T. Cheng, Y. H. Zhan, B. J. Huang, X. T. Gan, S. J. Li, S. H. Lin, X. F. Li, J. L. Zhao, H. D. Chen, Q. L. Bao, *Nanoscale* **2015**, *7*, 20249.
[228] D. Schall, M. Mohsin, A. A. Sagade, M. Otto, B. Chmielak, S. Suckow, A. L. Giesecke, D. Neumaier, H. Kurz, *Opt. Express* **2016**, *24*, 7871.
[229] C. Monat, Y. Su, *APL Photonics.* **2020**, *5*, 020402.

© 2020 WILEY-VCH Verlag GmbH & Co. KGaA, Weinheim